Technische Universität München

TUM School of Medicine and Health

Cell-cycle/ciliogenesis/UPR-autophagy hub defects impair cardiac progenitor specification in hypoplastic left heart syndrome

Vollständiger Abdruck der von der TUM School of Medicine and Health der Technischen Universität München zur Erlangung einer

Doktorin der Medizin (Dr. med.)

genehmigten Dissertation.

Ilaria My

Vorsitz: Prof. Kathrin Schumann, Ph.D.

Prüfer der Dissertation:

1. Prof. Dr. Karl-Ludwig Laugwitz
2. Prof. Dr. Andreas Dendorfer
3. Prof. Dr. Thomas Eschenhagen

Die Dissertation wurde am 09.05.2023 bei der Technischen Universität München eingereicht und durch die TUM School of Medicine and Health am 07.02.2024 angenommen.

Abstract

Introduction: Complex molecular programs in specific cell lineages govern human heart development. Congenital heart disease (CHD) is the result of abnormal heart development during organogenesis and is the most common developmental malformation, affecting almost 1% of live births. Hypoplastic left heart syndrome (HLHS) is the most common and severe manifestation of a spectrum of congenital left ventricular outflow tract obstruction defects occurring in association with ventricular hypoplasia. The current clinical paradigm assumes that the underlying aetiology of ventricular and aortic hypoplasia in HLHS is largely due to altered hemodynamic forces, with reduced blood flow and sheer stress and consequent underdevelopment of the heart.

Results and Discussion: Here, we performed induced pluripotent stem cells (hiPSCs)-based modeling, derived from HLHS patients, that demonstrated intrinsic defects in the cell-cycle/ciliogenesis/UPR-autophagy hub resulting in disrupted differentiation of early cardiac progenitor (CP) of first heart field (FHF) and second heart field (SHF) lineages. HLHS in vitro cellular models show specific transcriptional alterations in cardiac gene programs detected during early FHF CP specification and cardiomyocyte (CM) differentiation. This evidence suggests that the primary onset of the disease occurs at the initial stages of cardiogenesis when CM lineage decisions arise within CP populations. The experimental alterations observed in the cell-cycle/ciliogenesis/UPR-autophagy hub could be considered a common mechanism of delayed CP specification.

Conclusion: Our results highlight that despite genetic heterogeneity in HLHS, genetic perturbations converge on sequential cellular processes driving cardiogenesis and suggest novel therapeutic approaches to augment or replace surgical intervention.

Zusammenfassung

Einleitung: Komplexe molekulare Abläufe in spezifischen Zelllinien bestimmen die Entwicklung des menschlichen Herzens. Angeborene Herzfehler sind die Folge einer abnormalen Herzentwicklung während der Organogenese und die häufigste Entwicklungsfehlbildung, von der fast ein Prozent der Lebendgeburten betroffen sind. Das hypoplastische Linksherzsyndrom (HLHS) ist die häufigste und schwerwiegendste Manifestation eines Spektrums angeborener Obstruktionsdefekte des linksventrikulären Ausflusstrakts, die in Verbindung mit einer ventrikulären Hypoplasie auftreten. Das derzeitige klinische Paradigma geht davon aus, dass die zugrunde liegende Ätiologie der ventrikulären und aortalen Hypoplasie bei HLHS größtenteils auf veränderte hämodynamische Kräfte zurückzuführen ist, mit reduziertem Blutfluss und Sheer-Stress und daraus resultierender Fehlerentwicklung des Herzens.

Ergebnisse und Diskussion: Wir führten eine auf induzierten pluripotenten Stammzellen (hiPSCs) basierende Modellierung durch, die von HLHS-Patienten stammten und intrinsische Defekte im Zellzyklus/Ziliogenese/UPR-Autophagie-Hub aufwiesen, was zu einer gestörten Differenzierung des frühen kardialen Vorläuferzellen (CP) der Linien des ersten Herzfeldes (FHF) und des zweiten Herzfeldes (SHF) führte.

HLHS-In-vitro-Zellmodelle zeigen spezifische transkriptionelle Veränderungen in kardialen Genprogrammen, die, während der frühen FHF-CP-Spezifikation und Kardiomyozyten (KM)-Differenzierung nachgewiesen wurden. Diese Beweise deuten darauf hin, dass der primäre Beginn der Krankheit in den Anfangsstadien der Kardiogenese auftritt, wenn KM-Abstammungsentscheidungen innerhalb von CP-Populationen getroffen werden. Die beobachteten experimentellen Veränderungen im Zellzyklus/Ziliogenese/UPR-Autophagie-Hub könnten als gemeinsamer Mechanismus der verzögerten CP-Spezifikation angesehen werden.

Konklusion: Unsere Ergebnisse unterstreichen, dass trotz genetischer Heterogenität bei HLHS genetische Störungen auf sequenzielle zelluläre Prozesse konvergieren, die die Kardiogenese antreiben und sich hiervon möglicherweise neue therapeutische Ansätze in Zukunft ableiten lassen.

Table of contents

Abbreviations

AAF	Autophagy activity factor
ATF6	Activating transcription factor 6
ATG	Autophagy related genes/proteins
BMP	Bone morphogenetic protein
BSA	Bovine serum albumin
CHD	Congenital heart disease
CIM	Cardiac progenitor or Cardiomyocyte induction medium
CMs	Cardiomyocytes
CPs	Cardiac Progenitors
D-DNM	Damaging de novo mutations
DEGs	Differentially expressed genes
EBs	Embryoid bodies
ER	Endoplasmic reticulum
FBS	Fetal bovine serum
FGF	Fibroblast growth factor
FHF	First heart field
GATA4	GATA binding protein 4
GFP	Green fluorescent protein
Gli1	GLI Family Zinc Finger 1
GSK3β	Glycogen synthase kinase 3 β
HAND1	Heart And Neural Crest Derivatives Expressed 1
hiPSCs	Human induced pluripotent stem cells
HLHS	Hypoplastic left heart syndrome
IFT	Intraflagellar transport
IRE1α	Inositol-requiring enzyme 1α
ISL1	ISL LIM Homeobox 1
LC3B	Microtubule-associated protein 1A/1B-light chain 3
LV	Left ventricle
LVNC	Left ventricular non compaction cardiomyopathy
MESP1	Mesoderm Posterior BHLH Transcription Factor 1
NKX2-5	NK2 Homeobox 5
NOTCH1	Notch receptor 1
OFT	Outflow tract
PC	Primary cilium
PERK	Pancreatic EIF2-Alpha Kinase also known as Eukaryotic Translation Initiation Factor 2 Alpha Kinase 3 (EIF2AK3)
PFA	Paraformaldehyde
PTCH1	Patched 1
RIPA buffer	Radioimmunoprecipitation assay buffer
RV	Right ventricle
SAG	Sonic hedgehog signaling agonist
SDS-PAGE	Sodium Dodecyl Sulphate - PolyAcrylamide Gel Electrophoresis
SHF	Secondary heart field
Shh	Sonic hedgehog
SMO	Smoothened
TBX5	T-Box Transcription Factor 5
TGFβ	Transforming growth factor β
UPR	Unfolded protein response

1. Introduction

The heart is the first organ to form in the developing embryo and complex molecular and environmental cues converge in the specification of the multiple cellular lineages, contributing to chambers and circulatory system formation.
Heart development is timely and spatially regulated and is the result of an elegant fine-tuning of numerous essential signaling pathways and several biological processes. Understanding the biology behind cardiogenesis has always fascinated researchers in the field and has had a tremendous impact in advancing our current knowledge of congenital heart malformations.

The current investigation was conceived in order to explore and dissect the sequential cellular processes and their perturbations driving heart morphogenesis in one of the most severe congenital heart diseases, Hypoplastic Left Heart Syndrome. It is the result of a fruitful collaboration among internationally renowned groups with established expertise in heart development biology, molecular and clinical cardiology and cardiac surgery. The results obtained highlight new disease mechanisms arising in the early steps of cardiac progenitor differentiation and contributing to the final phenotype in the derived cardiomyocytes, that help to provide interesting insights into a complex disease, hopefully providing the basis for advancing knowledge in the field.

The present thesis will thoroughly describe the conceptual background and experimental work performed in the hypoplastic left heart syndrome patient-derived cellular models, in the laboratory directed from Prof. Laugwitz and Prof. Moretti. It can be described as a fascinating journey into molecular cardiology that deeply benefited from continuous sharing of ideas and experimental findings among group members, eventually leading to the final picture that we currently have.

1.1. Cardiogenesis

The mature heart arises from three major sources of embryonic progenitors, the cardiogenic mesoderm, the cardiac neural crest and the proepicardial organ, that give rise to all the cardiac structures and cellular components. Such progenitors become progressively restricted in their lineage potential, with peculiar temporal and spatial characteristics, that are tightly regulated and essential for giving ultimately rise to terminally differentiated cells of the heart.

The cardiogenic mesoderm forms the linear heart tube, which later gives rise to atrial and ventricular cardiomyocytes (CMs). The cardiac neural crest forms the smooth muscle cells of the aortic arch and the autonomic nervous system. Lastly, the proepicardium contributes to the formation of the coronary vasculature (Laugwitz KL. et al., 2008). The nearby endoderm is known to play a role in the activation of the cardiomyogenic transcriptional programs that activate important signals in heart development, like bone morphogenetic protein (BMP), fibroblast growth factor (FGF) and canonical and non-canonical WNT pathways, that are essential in the activation of key transcription factors like NK2 Homeobox 5 (*NKX2-5)*, ISL LIM Homeobox 1 (*ISL1)*, GATA binding protein 4 (*GATA4)* and T-Box Transcription Factor 5 (*TBX5)*.

Two main cardiac progenitor (CP) lineages contribute to the myocardium formation with two distinct cellular populations that provide different contributions to the developing working myocardium (Meilhac SM. et al., 2014). The first heart field (FHF) cells derive from the anterior lateral plate mesoderm and are the first to differentiate and give rise to the cardiac crescent and later the heart tube, ultimately forming the left ventricle (LV) and portion of the atria. On the other hand, the second heart field (SHF) cells are located medially to the cardiac crescent and show a delayed differentiation, constituting a reservoir of multipotent proliferative CPs (Kattman SJ. et al., 2006; Moretti A. et al., 2006), that will later give rise to the right ventricle (RV), the proximal outflow tract (OFT) and part of the atria (**Figure 1**). These cells are excluded from the early linear heart tube but migrate into the heart after looping of the heart tube has initiated, invading both the inflow and outflow tracts (Jain R. and Epstein JA. et al., 2018).

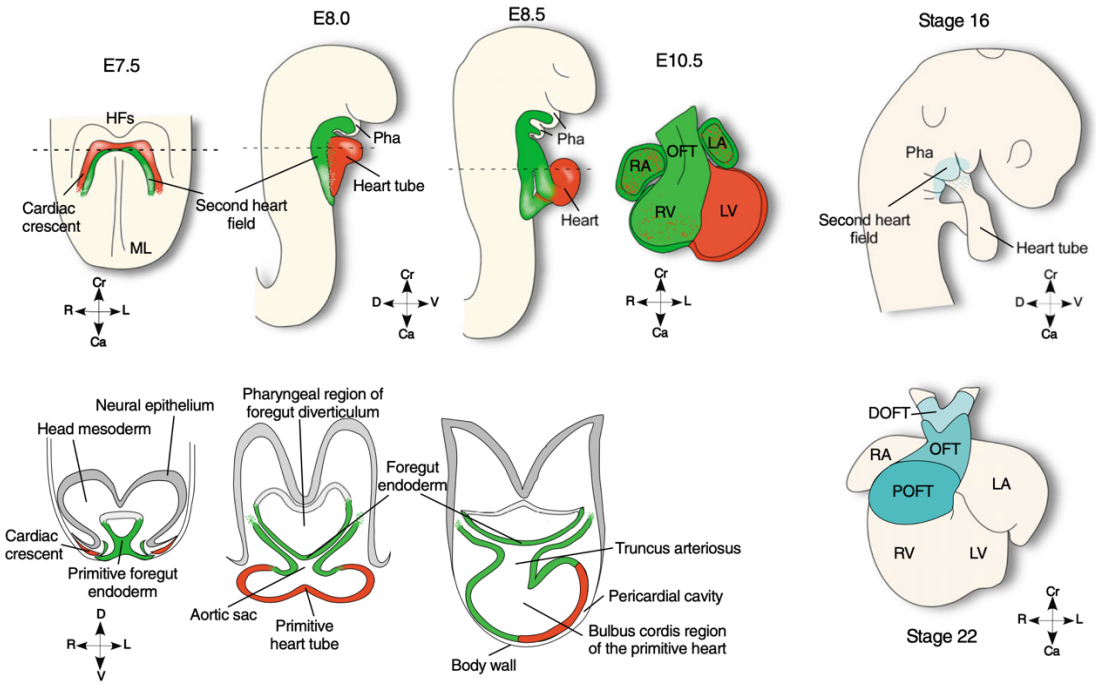

Figure 1. First and second heart fields and their contributions to the developing heart. The upper drawings show the relative position, movement and contribution of the SHF progenitors (green) relative to the FHF (red) from the cardiac-crescent through to the looping stages of mouse heart development. The dashed lines indicate the position of the corresponding sections shown in the lower panels. On the right side the location (upper) and contribution (beneath) of the SHF (blue) to the UFT in the chick embryo. *Source: Laugwitz, K.L., Moretti, A., Caron, L., Nakano, A., and Chien, K.R. (2008). Islet1 cardiovascular progenitors: a single source for heart lineages? Development 135, 193-205.*

Lineage tracing experiments have shown specific genetic signatures which identify the different subpopulations of CPs. The most primitive cellular components of the heart are marked by mesoderm posterior protein 1 (*MESP1)* expression, that is known to be required for the exit from the pluripotent state and the induction of the cardiovascular progenitor gene expression programs (Lescroart F. et al., 2018) (**Figure 2**).

MESP1+ expressing cells constitute early CPs and this transcription factor is expressed between E6.5 and E7.5 in mice. MESP1+ CPs will give rise to both FHF and SHF cells. Two key genes in the specification of the two heart fields are the homeobox transcription factors *NKX2-5* and *ISL1*. *NKX2-5* is expressed in both FHF and SHF cells, whereas *ISL1* marks primarily the SHF. Transient co-expression of both markers has been observed in early CPs (Moretti A. et al., 2006, Lescroart F. et al., 2018) and several works have shown that their reciprocal suppression allows subtype specification, expansion of ISL1+ CPs and differentiation into NKX2-5+ CMs (Dorn T. et al. 2015, Takeuchi JK. et al. 2005). FHF cells also express the T-box transcription factor *TBX5*

that is known to physically interact with *NKX2-5* (Bruneau BG. et al., 1999; Bruneau BG. et al., 2001).

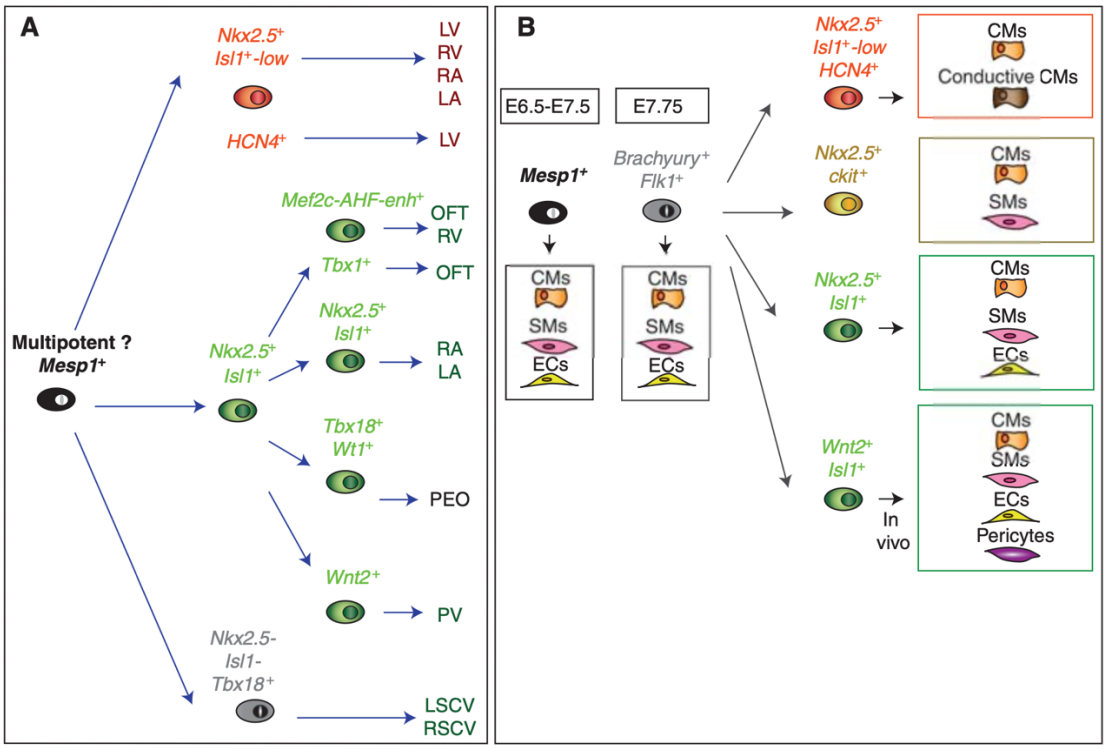

Figure 2. (A) Genetic origin of cardiac components, summarizing results from genetic tracing at the population level. (B) In vitro differentiation potential of cardiac precursors, summarizing results from clonal differentiation assays of embryonic cells or precardiac mesoderm, after cell sorting. CMs, cardiomyocytes; ECs, endothelial cells; LA, left atrium; LSCV, left superior caval vein; LV, left ventricle; OFT, outflow tract; PEO, proepicardial organ; PV, pulmonary vein; RA; right atrium; RSCV, right superior caval vein; RV, right ventricle; SMs, smooth muscle cells. *Source: Meilhac, S.M., Lescroart, F., Blanpain, C., and Buckingham, M.E. (2014). Cardiac cell lineages that form the heart. Cold Spring Harb Perspect Med 4, a013888.*

1.2. Congenital heart disease

Congenital heart disease (CHD) refers to abnormalities in heart structure and function that arise before birth (Bruneau BG., 2008). CHD is the result of abnormal heart development during organogenesis and is most common developmental malformation, affecting almost 1% of live births (Hoffman JI. and Kaplan S., 2002). They are usually clinically classified in cyanotic and non-cyanotic heart disease, as a result of the altered

blood oxygenation. Morbidity and mortality can deeply vary according to the severity of the disease.

Strong familial clustering has been demonstrated in CHD (Øyen N. et al., 2009) and supports the genetic etiology of the disease. Although single-gene mutation defects have been described in some cases, like the mutation of TBX5 in Holt-Oram syndrome, or the NKX2-5 mutation in atrial and ventricular septal defects, Tetralogy of Fallot and Ebstein anomaly (Bruneau BG., 2008), CHD presents mainly sporadic occurrence which supports underlying complex genetic mechanisms (Hinton RB. et al. 2007, Øyen N. et al., 2009, Preuss C. et al., 2016).
CHDs have been recapitulated in multiple experimental animal models by perturbing selected genes that function in the developmental pathways involved in cardiogenesis (Bruneau BG., 2008; Jain R. and Epstein JA. et al., 2018; Misra C. et al., 2014). However, the precise genetic, epigenetic, or environmental basis for these perturbations in humans remains poorly understood.

1.2.1 Hypoplastic left heart syndrome

Hypoplastic left heart syndrome (HLHS) - (MIM#241550) – is one of the most severe CHD, that is characterized by underdevelopment of the LV with atretic aortic and mitral valves (Lev M., 1952; Noonan JA. and Nadas AS., 1958). The resulting phenotype is characterized by a continuum of severity, that goes from a mild hypoplasia with a near normal LV, up to a rudimental LV that is unable to support the systemic circulation (**Figure 3**).

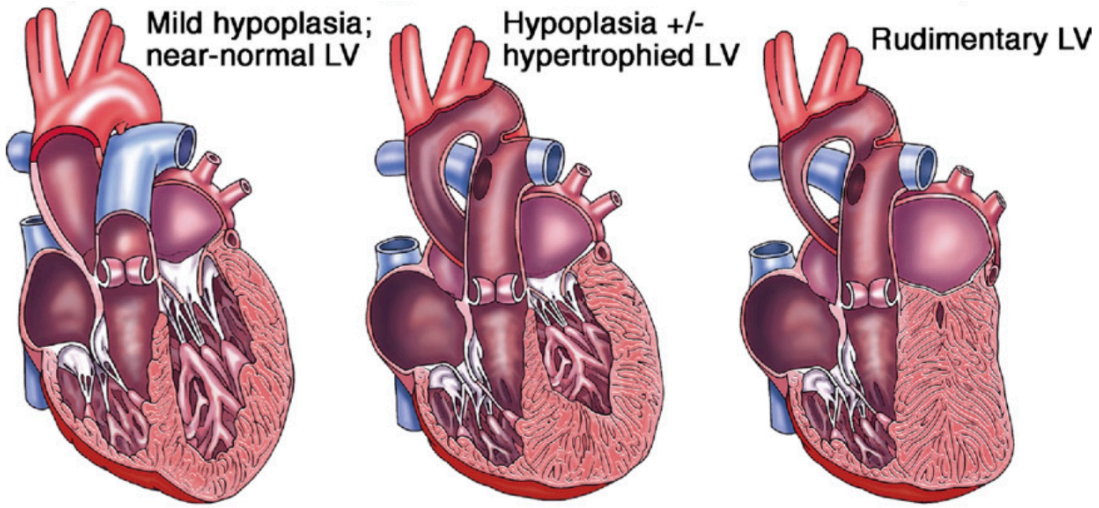

Figure 3. The hypoplastic left heart ventricle. LV = left ventricle. Source: Hickey, E.J., Caldarone, C.A., and McCrindle, B.W. (2012). Left ventricular hypoplasia: a spectrum of disease involving the left ventricular outflow tract, aortic valve, and aorta. *Source: J Am Coll Cardiol 59, S43- 54.*

Severe left ventricular hypoplasia requires immediate cardiac surgery after birth with Fontan procedure, that aims at allowing passive blood flow to the lungs and supporting the systemic circulation through the RV, or heart transplantation.

The underlying aetiology of the ventricular and aortic hypoplasia was originally attributed to altered hemodynamic forces, which were responsible for the reduced blood flow and sheer stress (Harh JY. et al, 1973; Hogers B. et al., 1997; Hickey EJ. et al., 2012). However, growing evidence is suggesting that a pathogenetic mechanism lying entirely on the "restricted flow theory" might be insufficient to fully explain the complex disease (Crucean A. at el., 2017). This is supported also by the inconsistent results obtained with the in utero aortic valvuloplasty, that was not efficient to fully restore the normal LV function (Freud LR. et al., 2014).

A seminal paper that changed our understanding of the biology behind HLHS was published in 2017 by Liu et al. (Liu X. et al., 2017), and was the first generation of HLHS mutant mice. New genes causing the disease were identified, and it was demonstrated that HLHS is multigenic and genetically heterogenous. Specific mutations, like Sap130, were proved to mainly affect LV trophism, with defects in proliferation and differentiation, weather some others, like Pcdha9, mainly caused aortic valve defects. Interestingly, transcriptional alterations found in mutant mice were present in both LV and RV, though less severe, suggesting intrinsic defect in myogenic programs.

1.3 Human induced pluripotent stem cells

The advent of somatic cell reprogramming (Takahashi K. et al., 2006), has brought great enthusiasm in the field of stem cell research and regenerative medicine, enabling the generation of human induced pluripotent stem cells (hiPSCs) from any individual carrying a disease and/or a specific mutation of interest.

Nowadays, hiPSCs are obtained thanks to the the overexpression of four reprogramming factors – *OCT4*, *SOX2*, *KLF4* and *c-MYC* – in somatic cells, usually peripheral blood mononuclear cells, through non integrating viral vectors. Several systems for high throughput differentiation to several cellular lineages and characterization of the obtained derivatives have been developed.

Multiple applications in disease modelling, drug and toxicity screening, tissue engineering or cellular transplantation have been developed (Pane LS. et al., 2016), contributing to great advancement of the knowledge in different fields of medicine (**Figure 4**).

hiPSCs offer the unprecedented opportunity to study *in vitro* the pathophysiology of human cardiogenesis, by direct comparison of the diseased cells, which carry the patient genetic background, to healthy control lines or even isogenic lines, which are obtained through genome editing techniques and differ from the patient line only for the mutation of interest.

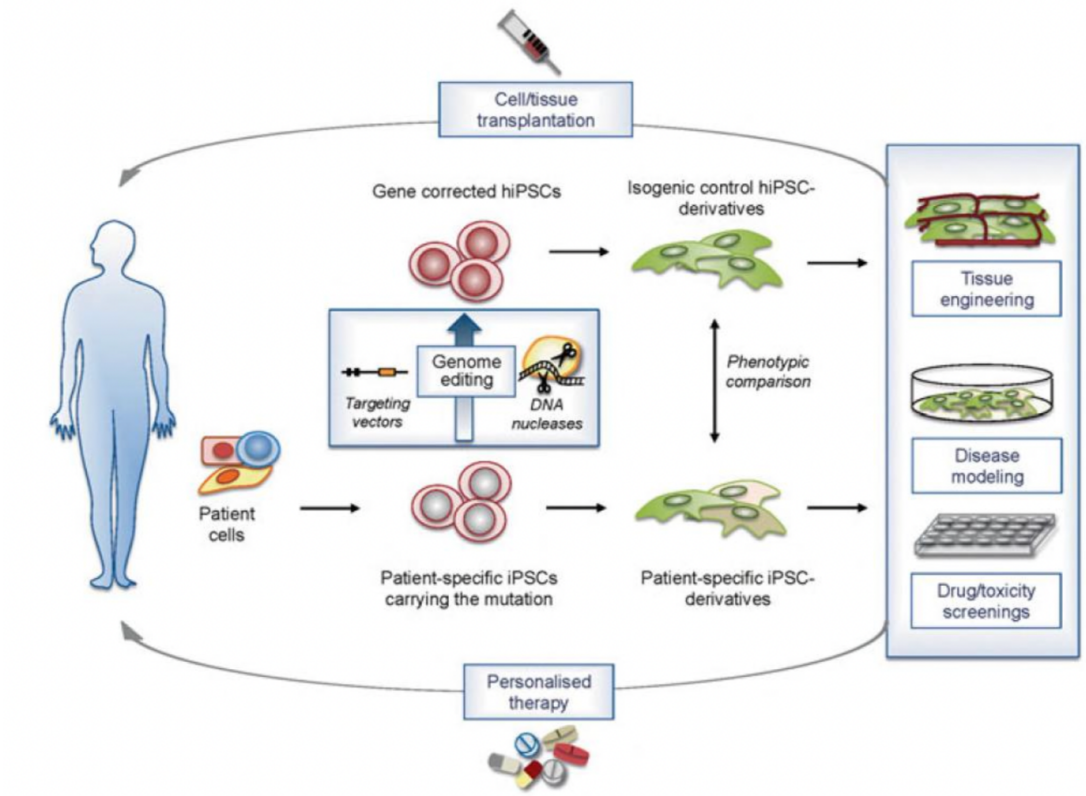

Figure 4. Schematic representation of the generation and application of induced pluripotent stem cell derivatives to disease modelling and therapeutic approaches. Source: Pane LS., My I., Moretti A. *Induced Pluripotent Stem Cells in Regenerative Medicine, Regenerative Medicine - from Protocol to Patient pp 51-75., Springer 2016.*

The *in vitro* differentiation of hiPSCs to cardiac derivatives follows the activation of signalling pathways that are known to play a crucial role during cardiogenesis *in vivo*, therefore this model systems can be considered a valuable tool for dissecting the molecular mechanisms in human cardiac development and function.

The first protocol that has been developed to produce CMs from hiPSCs was based on the formation of embryoid bodies (EBs) in suspension culture conditions and spontaneous differentiation to CMs. However, direct differentiation monolayer protocols have now been developed and enable generation of CMs with up to 90% efficiency. They are based on the addition of factors and small molecules that sequentially activate and inhibit the WNT signalling pathway. Briefly, they are characterized by initial addition of CHIR99021 to the culture medium, that is a selective GSK3β inhibitor, which activates WNT signalling; and later by addition of WNT inhibitor IWR1 that eventually drives the cells towards the cardiomyocyte fate. Several adaptations of this protocol originally published by Burridge et al. (Burridge PW. et al., 2014) have been developed, able to

specifically generate and focus on the cellular progenitor or mature subtype of interest. (Cao N. et al., 2013; Lee JH. et al., 2017; Protze SI. et al., 2017).

Recently, interesting works have applied the hiPSC technology to model CHD. For example, a heterozygous missense mutation in GATA4 associated with atrial and ventricular septal defects, has been shown to impair contractility, calcium handling and metabolic activity and disrupt TBX5 recruitment to cardiac super-enhancers, concomitant with dysregulation of genes related cardiac septation, in hiPSC-derived CMs (Ang YS. et a., 2016). Furthermore, hiPSC-CMs obtained from left ventricular non compaction cardiomyopathy (LVNC) patients carrying a mutation in the cardiac transcription factor TBX20 recapitulate a key aspect of the pathological phenotype at the single-cell level and this was associated with perturbed transforming growth factor beta (TGF-β) signalling (Kodo K. et al., 2016).

hiPSCs were also generated from patients with HLHS carrying NOTCH1 mutation or deleterious variants in NOTCH signalling pathway which presented altered CMs differentiation and sarcomeric structures and persistence of fetal gene expression patterns with activation of atrial gene programs (Hrstka SC. et al., 2017; Theis JL. et al., 2015; Yang C. et al., 2017; Jiang Y. et al., 2014). Another study showed transcriptional repression and epigenetic modification of NKX2-5, HAND1, and NOTCH1 (Kobayashi J. et al., 2014). Hypoxia has been postulated as a contributing factor, since LV in fetal HLHS samples demonstrates hypoxia-inducible factor-1α up-regulation, cellular senescence, TGF-β1eassociated fibrosis and impaired vasculogenesis. The phenotype was recapitulated by subjecting hiPSCs to hypoxia during cardiac differentiation and rescued by inhibition of TGF-β1 (Gaber N. et al., 2013).

Although several biological processes have been interestingly described in the HLHS cellular models in the above studies, what is still missing is a comprehensive picture of how the genetic heterogeneity finally converges in common alterations of cardiogenesis that eventually result in the final disease phenotype.

1.4 Primary cilium and cell cycle

Primary cilia (PC) are microtubular structures localized at the cell surface, highly conserved through evolution (Plotnikova OV. et al., 2009). They have been described in

several cell types and are known to play a role in embryonic development, cellular homeostasis and human disease.

Cilia are divided into two main categories, motile and non-motile cilia. Non motile cilia or PC present a structure with 9 doublets of microtubules, while motile cilia have an additional doublet with a final structure of 9 + 2. The ciliary axoneme has an essential role in assembly and disassembly of the PC and constitutes the main "road", through which intraflagellar transport proteins (IFT), kinesin (for the anterograde transport), dyneins (for the retrograde transport) and many other proteins move along the ciulium.

The basal body of the cilium is constituted by the centrioles that form the poles of the mitotic spindle during mitosis and there is a close interdependence of the ciliary machinery and the cell cycle. The PC is assembled during G1 and particularly G0 phases of the cell cycle, while it is disassembled during G2 and are absent in mitosis (**Figure 5**). Many cells produce PC after serum starvation, since it probably pushes entering of G0 phase and cell cycle exit. PC formation and cell cycle progression may reciprocally influence one another, although the exact mechanisms and the universality and exact dynamics of these mechanisms still remain to be fully elucidated (Santos N. et al., 2008).

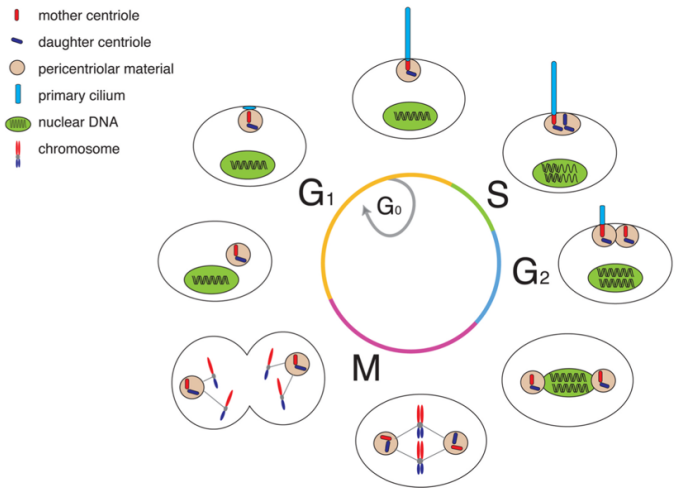

Figure 5. Primary cilium formation during cell cycle progression. *Source: Santos, N., and Reiter, J.F. (2008). Building it up and taking it down: the regulation of vertebrate ciliogenesis. Dev Dyn 237, 1972-1981.*

PC acts as a sensory antenna at the cell surface and is an essential player in the left-right patterning of the embryo and several signaling pathway receptors are docked at the ciliary membrane. The most well-known and characterized is the Sonic Hedgehog signaling (Shh), whose components are localized at the PC in mammals and abolition of

the cilia is known to also results in disruption of Shh signaling. Patched1, the receptor of Shh, in the absence of ligand inhibits smoothened, that is not able to activate Gli1 and Gli2 transcription factors, that are the ultimate players in the signaling cascade. Therefore, PC acts as a sensor of Shh ligand and activates the transduction of events that are crucial in cellular proliferation, stem cell specification and development. Other important signaling pathways in such biological processes are also known to be localized at these structures, like WNT, PDGF, TGF-b and BMP (Santos N. et al., 2008). A key role of the PC in neuroectodermal versus mesendodermal cell fate decisions has been described (Jang J. et al., 2016). The work by Li et al. (Li Y. et al., 2015), that performed a large-scale mutagenesis screening in mice, showed a centrale role for cilia in CHD. The majority of genes that were recovered in this work were related to cilia, suggesting an essential role of such structures in the pathogenesis of congenital heart malformations. This observation goes together with the well-known localization and activation at the level of the PC of crucial signaling pathways for heart formation. Similarly, patients with CHD show an enrichment in de-novo mutations related to PC.

1.5 Autophagy and primary cilium

Serum starvation is a condition that is known to trigger both PC formation and induction of autophagy. This common factor is the principle the pushed some researchers to explore the interconnection of the two cellular processes.

Autophagy is a process that is activated in order to catabolize proteins and organelles in double membrane structures, known as autophagosomes, that eventually fuse with lysosomes for degradation of the cargo, with the final goal of maintaining cellular homeostasis. Autophagy related proteins (ATG) play a key role in autophagosome formation, transport and docking with lysosomes.

A common marker of autophagic activity in cell culture is the measurement of conversion of LC3I to LC3II after conjunction with phosphatidylethanolamine, that integrates this protein into the membrane of the autophagosomes. Therefore, LC3I to II conversion quantification through immunofluorescence or immunoblotting is a reliable method to monitor autophagy.

Several studies have shown a tight dual interplay between autophagy and PC. PC and autophagy share part of the molecular machinery and common signaling pathways. For example, Shh activated from the cilia, is able to induce autophagy through the activation of autophagy related proteins that are located at the base of the PC. The pre-autophagosomal marker ATG16L1 is transported in IFT20-containing vesicles to the ciliary base, where autophagosomes may form from either the plasma membrane or the ciliary pocket (Pampliega O. and Cuervo AM., 2016) (**Figure 6**). Modulation of PC or autophagy was demonstrated to influence the other process in a bidirectional way. In particular, disruption of PC has a negative effect on autophagy as well, and inhibition of autophagy tends to increase PC growth and signaling activation but might also have the opposite effect according to the selective degradation of proteins that contribute to either the building or the reabsorption of the PC. After these observation Pampliega et al. (Pampliega O. et al., 2013) have proposed that basal autophagy is an important process in regulating growth and function of PC. The interconnection of such mechanisms might therefore be a central hub in human disease.

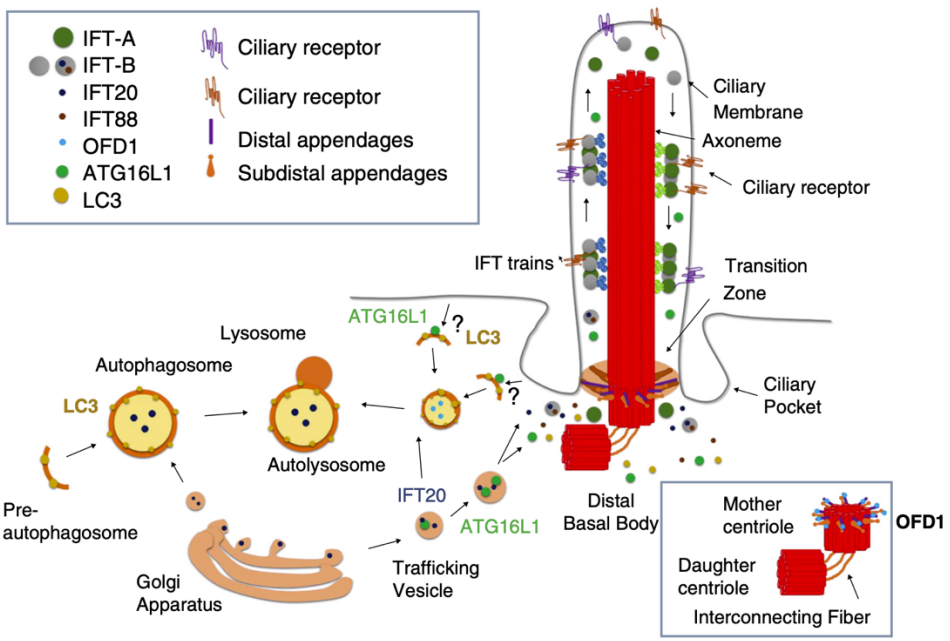

Figure 6. Molecular interaction between of autophagy and ciliogenesis. *Source: Pampliega, O., and Cuervo, A.M. (2016). Autophagy and primary cilia: dual interplay. Curr Opin Cell Biol 39, 1-7.*

1.6 Unfolded protein response

The endoplasmic reticulum (ER) is a cellular organelle where secretory and membrane proteins are synthesized and modified and is also a major intracellular calcium storage compartment inside the cell. Under physiological or pharmacological ER stresses, such as accumulation of misfolded proteins, or the treatment with chemicals that disrupt the ER-Golgi trafficking, the cells are able to activate the unfolded protein response (UPR) (Mao C. et al., 2006). UPR is also known to be able to trigger autophagy. Moreover, ER stress, similarly to autophagy, can occur under nutrient starvation.

UPR is a surveillance mechanism of protein homeostasis, that either is able to recover stress, or induces apoptosis. It plays a central role in lineage differentiation of embryonic and adult stem cells, impacting cell cycle progression and cellular specification (Heijmans J. et al., 2013; Xu H. et al., 2014). Laguesse et al. (Laguesse S. et al., 2015) have reported that UPR is able to control cell fate acquisition of neuronal progenitors during cortical neurogenesis. Moreover, evidence exists that UPR is critical during the early stages of cardiogenesis (Mao C. et al., 2006; Masaki T. et al., 1999).

Upon ER stress, UPR is transduced by de-repression of three ER transmembrane proteins: inositol-requiring enzyme 1a (IRE1α), double stranded RNA-dependent protein kinase-like ER kinase (PERK) and activating transcription factor 6 (ATF6) that work either alone or in concert to restore normal cellular function by controlling protein translation, folding and degradation (**Figure 7**) (Hetz C., 2012).

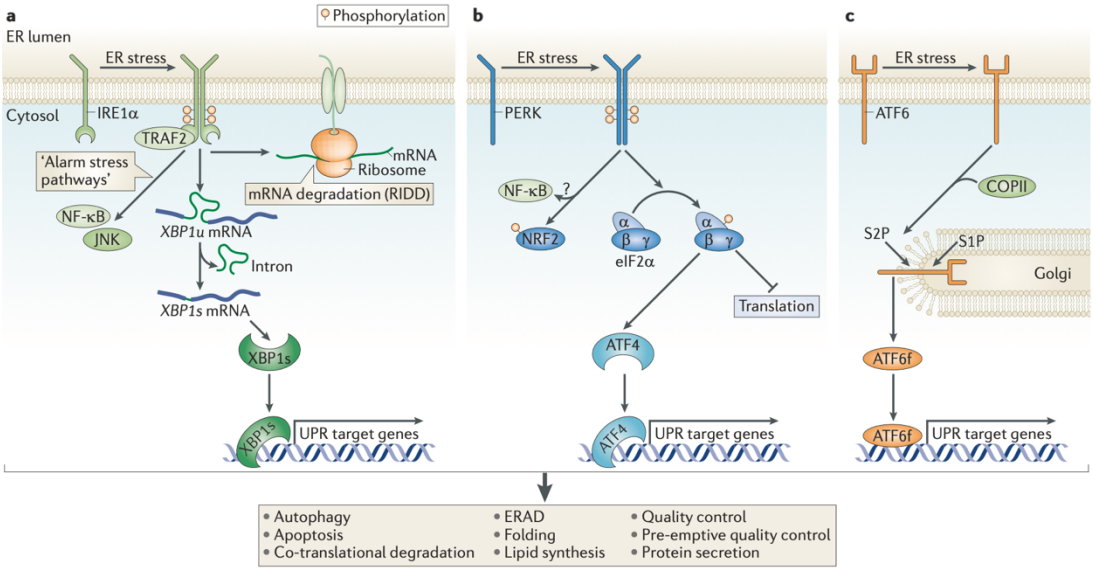

Figure 7. The UPR stress sensors (IRE1α, PERK and ATF6) transduce information about the folding status of the ER to the cytosol and nucleus to restore protein-folding capacity. *Source: Hetz C., Nat Rev Mol Cell Biol. 2012*

2. Methods

2.1. hiPSCs cell culture

The hiPSC lines were generated in the lab from 3 HLHS patients and 3 healthy subjects by reprogramming dermal fibroblasts or peripheral blood mononuclear cells using the CytoTune-iPS^{TM}-iPS 2.0 Sendai Reprogramming Kit (Thermo Fisher Scientific), as previously described (Gramlich M. et al., 2015; Moretti A. et al., 2020).
Several hiPSC clones from each HLHS patient and healthy control probands were manually picked and expanded for characterization.
Sendai virus detection in hiPSCs was performed by RT-PCR at passage 5 to 10. Expression of pluripotency markers in hiPSCs was verified by RT-PCR and immunostaining.
Spontaneous differentiation of hiPSCs into cells of all three germ layers was induced by embryoid body (EB) formation, as previously described (Moretti A. et al., 2010). Expression of lineage markers representative for three embryonic germ layers was assessed at day 21 of EB differentiation. Karyotyping and testing for karyotype-specific anomalies was done for all hiPSC lines.
hiPSCs were maintained in TeSR^{TM}-E8^{TM} medium on Matrigel or Geltrex-coated dishes and non-enzymatically passaged every 5–7 days after reaching 85–100% confluency using 0.5 mM EDTA/PBS solution. 10 μM Rock Inhibitor Y-27632 was added only for the first 24h after passaging.

2.2. CP differentiation protocol

For directed cardiac progenitor (CP) differentiation, hiPSCs were collected using Accutase (StemCell^{TM} Technologies) and plated on geltrex-coated dishes at a density of 5 × 104 cells/cm^2 in CP-induction medium (CIM), containing DMEM/F-12, 1 x B-27 Supplement without vitamin A, 2 mM L-glutamine, 100 U/mL penicillin, 100 μg/mL streptomycin and 400 μM 1-thioglycerol supplemented with 50 μg/mL ascorbic acid, 25 ng/mL recombinant human BMP4 and 3 μM CHIR99021 together with 10 μM Rock Inhibitor Y-27632 for the first 24 hours (Cao N. et al., 2013).

For primary cilia experiments, a higher seeding density (8.75 x 104 cells/cm^2) was used in order to obtain contact inhibition of proliferation and consequently a higher number of cells in G0 phase presenting the primary cilium at the day of the desired experiment. For cell cycle and proliferation analysis via flow cytometry, hiPSCs and CPs were dissociated using Accutase.

2.3. Shh, autophagy and UPR modulation on CPs

Sonic hedgehog signaling activation and inhibition was carried out by incubating CPs from day 1 to day 2 with 1 μM SAG smoothened agonist (Enzo Life Sciences) and 15 μM Cyclopamine (Sigma-Aldrich), respectively.

For autophagy stimulation, CPs were starved or treated at day 3 with 10 μg/ml brefeldin A for 6 hours. Inhibition of autophagy in control CPs was carried out by incubation at day 1.5 with 100 μM chloroquine (Sigma-Aldrich) for 12 hours.

For EIF2AK3 (PERK) activation, CPs were incubated for 6 hours with 5μM EIF2AK3 activator (CCT020312) at day 1.5 or day 3, as indicated.

2.4. CM differentiation protocol

hiPSCs were differentiated according the protocol of Burridge et al., 2015. Cells were dissociated using 0.5 mM EDTA/PBS solution and seeded as single cells on matrigel-coated plates in TeSR^{TM}-E8^{TM} until confluency attained 85-95%.
On day 0, cells were treated with 4-6 μM CHIR99021 (Selleckchem) in RPMI 1640 supplemented with B27 minus insulin.
On day 3, cells were treated with 2 μM Wnt-C59 (Selleckchem) in RPMI 1640 supplemented with B27 minus insulin.
By day 7, beating CMs were observed, and cells were switched to RPMI supplemented with B27.
For down-stream experiments, beating regions were manually dissected on day 15-18 and reseeded on fibronectin-coated dishes in EB2 medium (DMEM/F12 containing 2%

FBS, 1x MEM nonessential amino acids, 1x penicillin/streptomycin, 0.1 mM b-mercaptoethanol and 2 6 mM L-glutamine).
CMs were dissociated at the desired timepoint into single cells using 480 U/mL collagenase type II (Worthington).

2.5 RNA sequencing

Transcriptome profiling was performed by RNAseq on pooled RNA isolated from hiPSCs, hiPSC-derived CPs (at day 1, 2, and 3) and hiPSC-derived CMs (at day 6, 8, and 14) obtained from three independent differentiation experiments carried out in triplicates. Total RNA was isolated using the Absolutely RNA Microprep Kit (Agilent Technologies) and RNA quality was assessed on Agilent 2100 Bioanalyzer (Agilent Technologies) using Agilent RNA 6000 Nano Kit (Agilent Technologies). RNA-sequencing libraries were prepared from 1 μg RNA using TruSeq Stranded Total RNA Library Prep (Illumina). Samples were sequenced on the Illumina HiScan-SQ (Illumina). The reads were filtered for low-quality, contaminating 5′ adapters, homopolymers and trimmed for 3′ adapters. Quality control analysis was performed using FastQC, trimming of small 3' RNA adapter sequences, using Trimmomatic v0.36 with default parameters. Quality checked reads were then aligned to the human genome (GRCh37 assembly) using TopHat2 (default parameters). Gene annotation was obtained for all known genes in the human genome, as provided by Ensemble (GRCh37) (https://support.illumina.com/sequencing/se-quencing_software/igenome.ilmn). Using the reads mapped to the genome, the number of reads mapping to each transcript was calculated with HTSeq-count. Raw read counts were then used as input to DESeq2 v1.20.0. for calculation of size factor and scaling factor of normalized signal to bring the count values across all the samples to a common scale for each transcript. Subsequently data analysis was performed from the bioinformatic staff scientist.

2.6 Cell cycle, apoptosis, proliferation, and autophagy analysis by flow cytometry

Cell cycle analysis was based on the quantification of DNA content by propidium iodide (PI) using flow cytometry. hiPSCs, CPs (at day 1, 2, and 3) were dissociated with Accutase and fixed with ice-cold 70% ethanol for two hours on ice. Cells were then washed three times with PBS and incubated for 30 minutes with 200 µg/mL RNAse A (Qiagen) at room temperature. Subsequently, 1 mg/mL PI was added for 30 minutes at room temperature and samples were analyzed by flow cytometer. The G1 phase is characterized by the lower PI signal due to the lower DNA content, while the G2/M phase is characterized by double DNA content corresponding to a higher PI signal intensity. (see Figure 11 C).

For quantification of proliferation, hiPSCs and CPs (at day 1, 2, and 3) were incubate with 10 µM EdU for two hours, dissociated with Accutase, fixed with 4% paraformaldehyde (PFA) for 15 min at 20 room temperature, washed three times with PBS and processed using the Click-iT EdU Alexa Fluor 488 Flow Cytometry Assay Kit (Thermo Fisher Scientific) according to manufacturer's instructions. The samples were then subjected to immunostaining with rabbit anti-cleaved caspase 3 antibody (Cell Signaling Technology) overnight at 4°C, followed by incubation with secondary antibody anti-rabbit AlexaFluor-Pacific-Blue for one hour at room temperature.

For detection of autophagic flux, CPs were dissociated at day 3 and processed using Cyto-ID™ Autophagy Detection Kit 2.0 (Enzo Life Sciences) according to manufacturer's instructions. The autophagy activity factor (AAF) was calculated based on mean fluorescence intensity of autophagic vacuoles as described by Chan LL. et al., 2012. Flow cytometry acquisition analysis was performed with Gallios (Beckman Coulter) and data were evaluated with Kaluza software (Beckman Coulter).

2.7 Immunocytochemistry

For primary cilium staining, CPs were fixed with 4% PFA for 10 minutes at room temperature, permeabilized with 0.1 M glycine in PBS/0.2% Triton-X-100 for 10-20 minutes, blocked with PBS/0.1% Tween-20 containing 10% FBS, 0.1% BSA and 3%

donkey serum for 2 hours at room temperature. Samples were incubated with primary antibodies for acetylated tubulin (Sigma-Aldrich) and pericentrin (Covance) in PBS/0.1% Tween-20 containing 1% FBS, 0.1% BSA and 3% donkey serum overnight at 4°C. Next day, secondary antibodies AlexaFluor488-donkey anti-mouse IgG (Thermo Fisher Scientific) and AlexaFluor-594-donkey anti-rabbit (Thermo Fisher Scientific) were incubated in PBS/0.1% Tween-20 containing 1% FBS, 0.1% BSA and 3% donkey serum for one hour at room temperature.

For LC3B staining, CPs were incubated for 6 hours with 50μM chloroquine before fixation with 4% PFA for 10 minutes at room temperature, permeabilized with 100% ice cold methanol for 10 min at −20 °C and washed three times with PBS. After blocking with 3% BSA/PBS for 30 minutes at room temperature, samples were incubated with LC3 antibody (1:100) in 3% BSA/PBS over-night at 4°C. Next day, secondary antibody AlexaFluor-488-donkey anti-rabbit IgG (Thermo Fisher Scientific) was incubated in 3%BSA/PBS for 1 hour at room temperature.

Images were acquired using an SP8 II confocal laser-scanning Leica microscope. Images were assigned with pseudo-colors and processed with ImageJ or Adobe Photoshop. For quantification of TBX5, ISL1, NKX2-5 immunolabeled CPs, marker intensity was measured using Image-J software, applying the same acquisition settings and exposure. The cutoffs for high and low were determined according to the mean intensity level of each marker, excluding statistically significant outliers.

Area of the LC3-positive puncta was semiautomatically quantified using a NIH ImageJ macro (GFP-LC3) developed specifically for this purpose (Chu CT. et al., 2009; Dagda RK. et al., 2008). For each cell, the overall area of LC3-positive puncta was expressed as a percentage of the area of the whole cell.

2.8 Western blotting

Protein samples of CPs were prepared using RIPA buffer (Sigma-Aldrich), separated by SDS-PAGE and blotted according to standard protocols. For LC3 detection, cells were incubated for 6 hours with 50μM chloroquine before lysis and a 4-20% polyacrylamide gradient gel (Bio-Rad) was used. Incubation with primary antibodies against GLI1 (Abcam), eIF2α (Cell Signaling Technology), Phospho-eIF2α (Ser51) (Cell Signaling Technology), LC3 (Novus Biologicals), p62 (Enzo Life Sciences), and GAPDH (Cell

Signaling Technology) was performed overnight at 4°C. HRP-conjugated secondary antibodies (Jackson Immunoresearch) were applied next day for one hour. Protein band intensity was quantified using ImageJ.

2.9 RNA isolation and quantitative real-time PCR

RNA was isolated using the Absolutely RNA Microprep Kit (Agilent Technologies) and 1 μg was used to synthesize cDNA with the High-Capacity cDNA Reverse Transcription kit (Applied Biosystems). Gene expression was quantified by qRT-PCR using 1 μL cDNA and the Power SYBR Green PCR Master Mix (Applied Biosystems). Gene expression levels were normalized to GAPDH. Full list of olinucleotides used is provided in Table below.

2.10 Statistical analysis

Statistical analyses were performed using R environment. Data that passed tests for normality were analyzed with the use of t-tests for equal (Student's t-test) or unequal (Welch's t-test) variances. For data that were not normally distributed, a Mann–Whitney U-test was applied. P values of less than 0.05 were considered statistically significant. Unless otherwise stated, all data are shown as means ± SEM.

Antibodies	Company	Catalogue #
Primary antibodies		
Anti-Acetylated Tubulin antibody, mouse monoclonal antibody	Sigma-Aldrich	T7451
Anti-Cleaved Caspase-3 (Asp175) (5A1E), rabbit monoclonal antibody	Cell Signaling Technology	9664
Anti-eIF2α, rabbit monoclonal antibody	Cell Signaling Technology	5324
Anti-GAPDH (14C10), rabbit monoclonal antibody	Cell Signaling Technology	2118S
Anti-GLI1, rabbit monoclonal antibody	Abcam	ab134906
Anti-ISL1, mouse monoclonal antibody	Developmental Studies Hybridoma Bank	39.4D5
Anti-LC3B, rabbit polyclonal antibody	Novus Biologicals	NB100-2220
Anti-NKX2.5, goat polyclonal antibody	Novus Biologicals	NBP1-51953
Anti-p62, rabbit polyclonal antibody	Enzo Life Sciences	BML-PW9860-0100
Anti-Pericentrin, rabbit polyclonal antibody	Covance	PRB-432C
Anti-Phospho-eIF2α (Ser51), rabbit monoclonal antibody	Cell Signaling Technology	3398
Anti-PTCH1, rabbit polyclonal antibody	LSBio	LS-C176173
Anti-TBX5, rabbit polyclonal antibody	Abcam	ab137833
Secondary antibodies		
Donkey anti-Goat IgG (H+L) Cross-Adsorbed Secondary Antibody, Alexa Fluor 594	Thermo Fisher Scientific	A-11058
Donkey anti-Mouse IgG (H+L) Highly Cross-Adsorbed Secondary Antibody, Alexa Fluor 488	Thermo Fisher Scientific	A-21202
Donkey anti-Rabbit IgG (H+L) Highly Cross-Adsorbed Secondary Antibody, Alexa Fluor 594	Thermo Fisher Scientific	A-21207
Donkey anti-Rabbit IgG (H+L) Highly Cross-Adsorbed Secondary Antibody, Alexa Fluor 647	Thermo Fisher Scientific	A-31573
Goat anti-Mouse IgG (H+L) Cross-Adsorbed Secondary Antibody, Alexa Fluor 594	Thermo Fisher Scientific	A-11005
Goat anti-Mouse IgG (H+L) Cross-Adsorbed Secondary Antibody, Alexa Fluor 647	Thermo Fisher Scientific	A-21235
Goat anti-Mouse IgG (H+L) Highly Cross-Adsorbed Secondary Antibody, Alexa Fluor 488	Thermo Fisher Scientific	A-11029
Goat anti-Mouse IgG H&L (Alexa Fluor® 488)	Abcam	ab150121
Goat anti-Mouse IgG H&L (Alexa Fluor® 555)	Abcam	ab150114
Goat anti-Rabbit IgG (H+L) Cross-Adsorbed Secondary Antibody, Alexa Fluor 488	Thermo Fisher Scientific	A-11008
Goat anti-Rabbit IgG (H+L) Cross-Adsorbed Secondary Antibody, Alexa Fluor 647	Thermo Fisher Scientific	A-21244
Goat Anti-Rabbit IgG H&L (Alexa Fluor® 488)	Abcam	ab150077
Goat Anti-Rabbit IgG H&L (Alexa Fluor® 555)	Abcam	ab150078
Goat-anti Mouse IgM (Alexa Fluor® 488)	Abcam	ab150121
Peroxidase AffiniPure Donkey Anti-Mouse IgG (H+L)	Jackson Immunoresearch	715-035-151
Peroxidase AffiniPure Goat Anti-Rabbit IgG (H+L)		
Peroxidase AffiniPure Goat Anti-Rabbit IgG (H+L)	Jackson Immunoresearch	111-035-144

Table 1. List of primary and secondary antibodies used in the study.

Chemicals, Peptides, and Recombinant Proteins	Company	Catalogue #
1-Thiolycerol	Sigma-Aldrich	M6145
Accutase	StemCell Technologies	7920
B27 Supplement (50x)	Thermo Fisher Scientific	17504044
B27 Supplement (50x), Minus Insulin	Thermo Fisher Scientific	A1895601
B27 Supplement (50x), Minus Vitamin A	Thermo Fisher Scientific	12587010
BMP4, human recombinant	R&D Systems	314-BP
Brefeldin A	Sigma-Aldrich	B6542
BSA, Bovine Albumin Fraction V	Thermo Fisher Scientific	15260
CHIR99021	Selleckchem	S2924
Chloroquine diphosphate salt	Sigma-Aldrich	C6628
Collagenase Type II	Worthington	LS004177
Corning® Matrigel® Growth Factor Reduced (GFR) Basement Membrane Matrix	Corning	356231
Cyclopamine hydrate	Sigma-Aldrich	C4116
DMEM/F12 medium	Thermo-Fisher Schientific	21331020
EDTA, 0.5 M, pH 8.0	Thermo-Fisher Schientific	15575-038
EIF2AK3 (PERK) Activator, CCT020312	Sigma-Aldrich	324879
FBS	Thermo-Fisher Schientific	10270106
Fibronectin	Sigma-Aldrich	F1141
Geltrex	Thermo-Fisher Schientific	A1413302
L-Ascorbic acid	Sigma-Aldrich	A5960
L-Glutamine 200 mM	Thermo-Fisher Schientific	25030024
MEM Nonessential amino acids (100X)	Thermo-Fisher Schientific	11140050
Paraformaldehyde	Sigma-Aldrich	P6148
Penicillin/Streptomycin, 100x	Thermo-Fisher Schientific	15140122
Propidium iodide	Sigma-Aldrich	P4864
RIPA buffer	Sigma-Aldrich	R0278
RNAse A, DNAse-free	Qiagen	79254/1581922
Rock Inhibitor Y-27632	Merck Millipore	SCM075
RPMI 1640	Thermo-Fisher Schientific	11875-119
SAG smoothened ligand	Enzo Life Sciences	ALX-270-426
Serum, normal donkey	Abcam	ab7475
Serum, normal goat	Abcam	ab7841
Sodium dodecyl sulfate	Merck Millipore	L6026
TeSR™-E8™	StemCell™ Technologies	05990
Triton-X-100	Sigma-Aldrich	T8787
Tween-20	Sigma-Aldrich	P2287
Wnt-C59	Selleckchem	S7037
b-mercaptoethanol	Thermo Fisher Scientific	35602BID

Table 2. List chemicals, peptides and recombinant proteins used in the study.

Critical commercial assays	Company	Catalogue #
Agilent Absolutely RNA Microprep Kit	Agilent Technologies	400805
Agilent RNA 6000 Nano Kit	Agilent Technologies	5067-1511
Chromium i7 Multiplex Kit	10x Genomics	PN-120262
Chromium Single Cell 3' Library & Gel Bead Kit v2	10x Genomics	PN-120237
Chromium Single Cell A Chip Kit	10x Genomics	PN-120236
Click-iT EdU Alexa Fluor 488 Cell Proliferation Kit for Imaging	Thermo Fisher Scientific	C10337
Click-iT EdU Alexa Fluor 488 Flow Cytometry Assay Kit	Thermo Fisher Scientific	C10425
CYTO-ID® Autophagy detection kit 2.0	Enzo Life Sciences	ENZ-KIT175
High-Capacity cDNA Reverse Transcription Kit	Thermo Fisher Scientific	4368814
Power SYBR® Green PCR Master Mix	Applied Biosystems	4367659

Table 3. List of critical commercial assays used in the study.

Oligonucle-otides	Forward	Reverse
ARL13b	5'-GAACCAGTGGTCTGGCTGAGTT-3'	5'-GTTTCAGGTGGCAGCCATCACT-3'
ATG3	5'-ACTGATGCTGGCGGTGAAGATG-3'	5'-GTGCTCAACTGTTAAAGGCTGCC-3'
ATG5	5'-GCAGATGGACAGTTGCACACAC-3'	5'-GAGGTGTTTCCAACATTGGCTCA-3'
ATG12	5'-GGGAAGGACTTACGGATGTCTC-3'	5'-AGGAGTGTCTCCCACAGCCTTT-3'
CHOP	5'-GGAACCTGAGGAGAGAGTGTTC-3'	5'-TTTTGGAAAAGGGTAGGTTAAGTTT-3'
EIF2AK3 (PERK)	5'-GTCCCAAGGCTTTGGAATCTGTC-3'	5'-CCTACCAAGACAGGAGTTCTGG-3'
GAPDH	5'-TCCTCTGACTTCAACAGCGA-3'	5'-GGGTCTTACTCCTTGGAGGC-3'
GLl1	5'-AGCCTTCAGCAATGCCAGTGAC-3'	5'-GTCAGGACCATGCACTGTCTTG-3'
GLI2	5'-GTCAGAGCCATCAAGACCGAGA-3'	5'-GCATCTCCACGCCACTGTCATT-3'
GLI3	5'-TCAGCAAGTGGCTCCTATGGTC-3'	5'-GCTCTGTTGTCGGCTTAGGATC-3'
IFT52	5'-CTTTACCACCCTCTTCGACCTG-3'	5'-GCGTCTCAAACTGAGGCTGGAT-3'
IFT88	5'-TCGGCTAGATGAGGCTTTGGAC-3'	5'-CACTGACCACCTGCATTAGCCA-3'
ISL1	5'-AAAGTTACCAGCCACCTTGGA-3'	5'-ATTAGAGCCCGGTCCTCCTT-3'
NKX2-5	5`-CACCGGCCAAGTGTGCGTCT-3'	5'-GCAGCGCGCACAGCTCTTTC-3'
PTCH1	5'-GCTGCACTACTTCAGAGACTGG-3'	5'-CACCAGGAGTTTGTAGGCAAGG-3'
SMO	5'-TGCTCATCGTGGGAGGCTACTT-3'	5'-ATCTTGCTGGCAGCCTTCTCAC-3'
Spliced-XBP1	5'-TGCTGAGTCCGCAGCAGGTG-3'	5'-GCTGGCAGGCTCTGGGGAAG-3'
TBX5	5'-GGGCAGTGATGACATGGAG-3'	5'-GCTGCTGAAAGGACTGTGGT-3'
Total-XBP1	5'-CTGCCAGAGATCGAAAGAAGGC-3'	5'-CTCCTGGTTCTCAACTACAAGGC-3'
ULK3	5'-CTACGCCAAGAAGGACACTCGT-3'	5'-ATCTCCGTGAGGAGGTTCTCCA-3'

Table 4. List of oligonucleotides used in the study.

3. Results

hiPSCs from 3 HLHS patients and 3 healthy subjects were previously generated in the laboratory using non integrating Sendai-virus reprogramming technique. All cell lines were thoroughly characterized and presented pluripotent stem cell characteristics and normal karyotypes.

The selection of HLHS patients for hiPSCs generation was based on the following criteria:

i) identical echocardiographic LV phenotype with normal wall thickness and large lumen.
ii) presence of damaging de novo (D-DNM) mutations in genes that were affected twice or belonged to a multi-hit gene family in the whole-exome sequencing previously performed on 87 patients with isolated HLHS and their parents.
iii) availability of fibroblasts for cell reprogramming.

Due to the multigenic aetiology of the disease we preferred to conduct unsupervised, genome-wide Omics analyses in multiple lines, rather than focusing on selected de novo mutations in isogenic controls that would have restricted the observation to single variants, without keeping into account the genetic background.

In the present work we combined transcriptome profiling of HLHS patients-derived CPs and CMs to decode cellular and molecular alterations behind the disease phenotype.

Our result show that the cell cycle/UPR-autophagy/ciliogenesis hub leads to disrupted differentiation of early FHF/SHF CP lineage commitment that is consequently translated into inability of the immature ventricular myocytes to respond to environmental cues essential for development growth.

Together, our results provide evidence of a cell-autonomous pathogenesis for HLHS, that supports the evidence that this CHD cannot be considered merely of hemodynamic origin, and provide novel potential nodes for therapeutic intervention.

3.1 RNA-Sequencing in CPs and CMs

Stepwise differentiation protocols were used in order to obtain early CPs (Cao N. et al., 2013) and CMs (Burridge PW. et al., 2014) (**Figure 8A**) from HLHS and control hiPSC lines. Both protocols are based on a transient initial activation of WNT signaling, through CHIR99021, a selective GSK3β inhibitor, supplemented with ascorbic acid and BMP4 in the CP differentiation protocol. All the lines responded to differentiation cues and were able to differentiate to the expected cellular derivatives.

RNA sequencing was performed at different stages during differentiation, that was D0, D1, D2 and D3 of CP protocol and D6, D8 and D14 of CM protocol. GSEA was used to determine any differences in gene expression between HLHS and healthy control cells at each timepoint (**Figure 8B**).

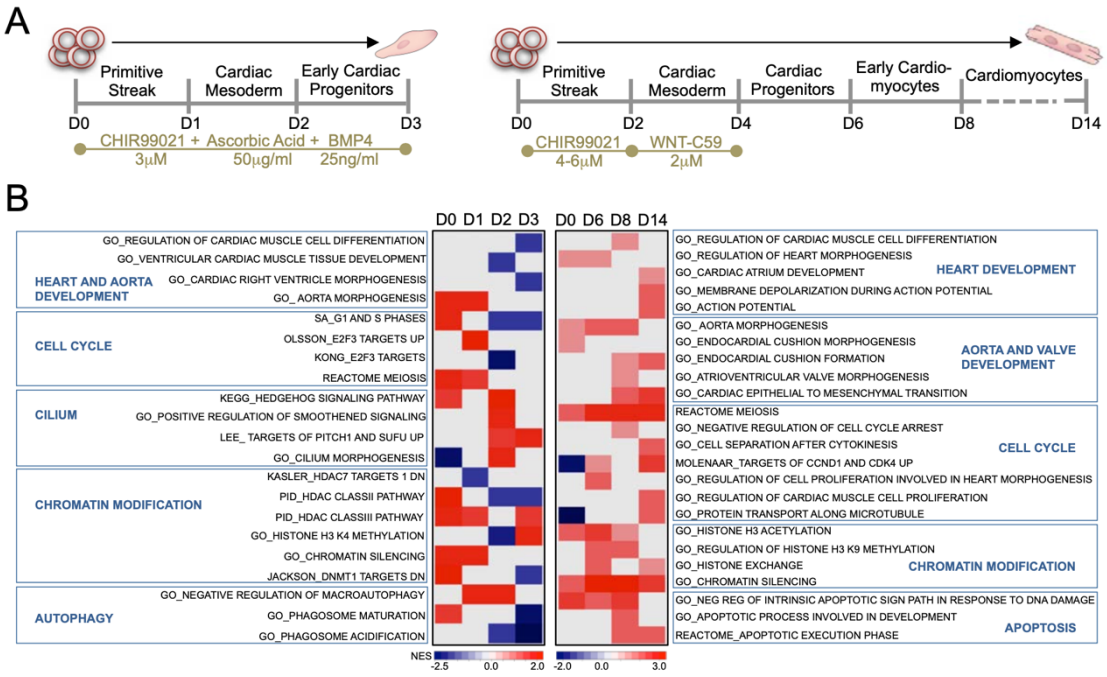

Figure 8. Gene expression analysis during iPSC-based cardiogenesis. (A) Directed hiPSC cardiac differentiation protocols used to generate CPs and CMs. (B) Heatmap of normalized enrichment scores (NES) for selected GSEA terms. Red and blue denotes terms with positive and negative NES, respectively.

We detected dynamic alterations in several gene categories that were common in both protocols, including those related to heart and aorta development, cell cycle and chromatin modification. Aberrations in cell cycle and autophagy were only present in early

CP, while apoptosis was solely affected in more mature CPs, starting from D6 and in D8 and D14 CMs.

Interestingly, in D2 and D3 CPs, detailed analysis of differentially expressed genes (DEGs) (1.5-fold expression, p-value ≤0.05) involved in cardiac development revealed that genes expressed in committed myocytic precursors and important for heart tube formation (such as ID2, TPM2, XIRP1, SRF, ETV1) were downregulated in HLHS, while genes involved in anterior/posterior patterning (HOXB9) and in vessel and valve development (VEGFB, TGFB2, GATA5) were upregulated (**Figure 9**). Transcripts typical of early CPs were decreased at D2, but augmented at D3, together suggestive of incomplete or delayed CP lineage specification. Concordantly, at D8 and D14, HLHS CMs showed upregulation of genes distinctive of myocytic progenitors/early immature CMs and altered expression of transcripts important for OFT and atrioventricular-canal (AVC), such as MEIS1, ISL1, TGFB2, and JUN, as well as heart chamber development (NR2F1, WNT2, ETV2, RXRA) (**Figure 9**), supporting a retarded and altered lineage-specific CM differentiation.

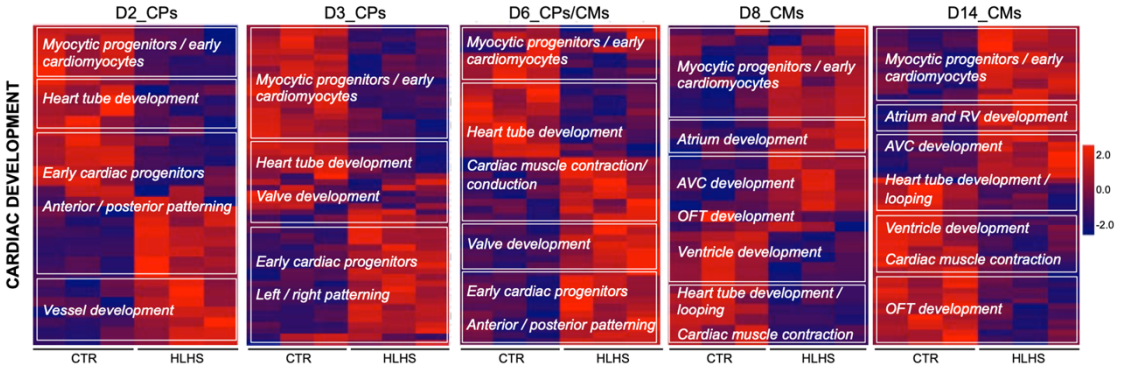

Figure 9. Heatmaps showing gene expression of DEGs involved in cardiac development at the indicated days of differentiation. Values are row-scaled to show their relative expression. Blue and red are low and high levels respectively.

Beside heart development, another process that recurrently emerged affected in our genome-wide analyses of HLHS was "cell cycle and proliferation". Cell cycle lengthening in G1 phase is linked to embryonic stem and progenitor cell differentiation (Lange C. and Calegari F., 2010). Moreover, CM maturation is accompanied by cell cycle withdrawal (Ikenishi A. et al., 2012). In CPs at D3, 74 of the 890 DEGs (8%) related to cell cycle and belonged to enriched pathways "Mitotic G1-G1/S phases", "M/G1 transition" "G1/S transition", and "cell cycle checkpoints" (**Figure 10 A**). Thirty-four of them gen-

erated a functional interactome network encompassing cell cycle interphase pathways as the top enriched, with most leading genes being downregulated (**Figure 10 B**).

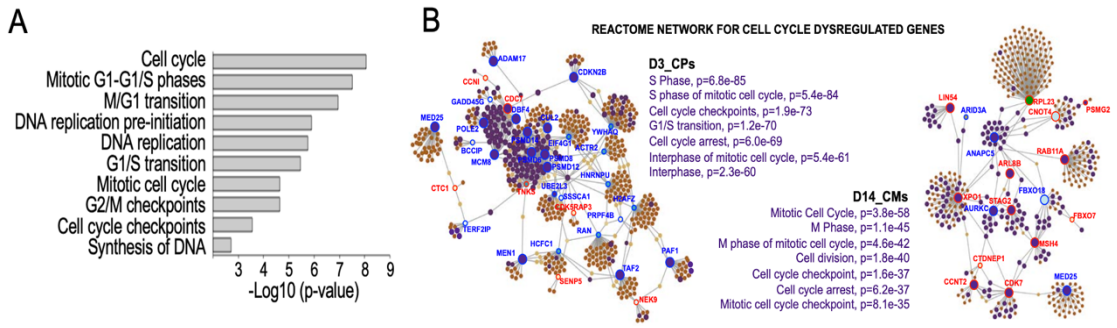

Figure 10. Cell cycle related DEGs in HLHS lines. (A) Top-ten enriched GO pathways from cell cycle DEGs of HLHS CPs at D3. (B) Networkanalyst-generated Protein-Protein interactome of DEGs involved in cell cycle at D3 and D14. Upregulated (red) and downregulated (blue) genes are shown. In purple are highlighted the genes belonging to the enriched GO categories specified on the side of the plots. Protein–protein interactions are indicated as solid grey lines between genes.

In CMs at D14, cell cycle DEGs (42 out of 754) generated 18 functional interaction nodes; top enriched terms within the interactome and regulation of the leading genes pointed to alteration in M phase, with active separation of chromatids (STAG2, XPO1) but defective progression through mitosis (ANAPC5) and cytokinesis (AURKC) (**Figure 10 B**). Together, the specific transcriptional alterations in cardiac gene programs detected during early CP specification and CM differentiation of HLHS iPSCs suggest the primary onset of the disease occurs at the initial stages of cardiogenesis when CM lineage decisions arise within CP populations.

3.2 Cell cycle patterning and early CPs specification

Considering the peculiar gene expression profile observed in HLHS lines, we proceeded to functionally characterize cell cycle phase distribution and markers of early CP specification in HLHS lines.

Embryonic stem cells have a unique cell cycle pattern distribution characterized by a short G1 phase that lengthens with differentiation (White J. and Dalton S., 2005). Their differentiation capacity and cell fate decisions are tightly associated with the cell cycle machinery (Pauklin S. and Vallier L., 2013). Therefore, we analysed cell cycle patterns

during early CP formation and compared them with the emergence of CP lineages marked by ISL1, NKX2-5, and TBX5. While control lines demonstrated a G1 lengthening starting between D1 and D2, patient lines prolonged the G1 phase with a 24h delay (**Figure 11**).

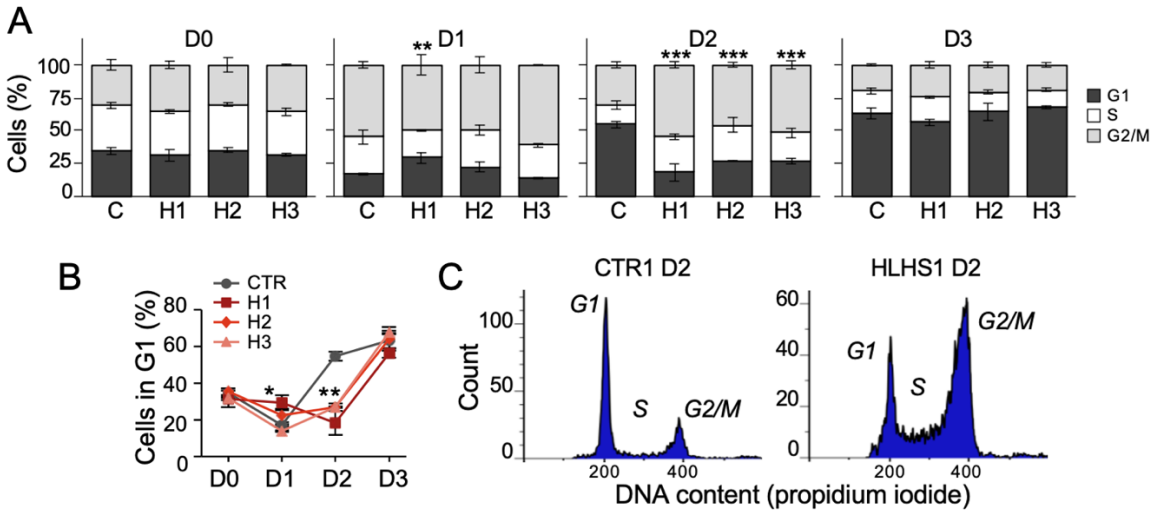

Figure 11. Analysis of cell cycle phase distribution in HLHS and control lines. (A) Propidium iodide staining analysis of HLHS (H) and control cells (C) during CP differentiation. (B) Percentage of cells in G1 during CP differentiation. (C) Representative FACS plots of D2 CPs from CTR1 and HLHS1 after staining with propidium iodide. Data are mean ± SEM, n=3 differentiations per line. *p<0.05, **p<0.005, ***p<0.001 (Chi-square test in panel A, t-test in panel B).

Concurrently, at D1, activation of ISL1 and NKX2-5 transcripts was dramatically reduced in HLHS (**Figure 12 A**) and correlated with a significant lower proportion of cells expressing ISL1 and NKX2-5 proteins at D2 (**Figure 12 B**), supportive of a retarded CP specification. Interestingly, four patterns of ISL1 and NKX2-5 expression were detected at D3: i) ISL1^{low}/NKX2-5^{low}, representing "early committed CPs"; ii) ISL1^{high}/NKX2-5^{high}, denoting "fully committed early CPs"; iii) ISL1^{high}/NKX2-5low, typical of SHF progenitors; and iv) ISL1^{low}/NKX2-5^{high}, distinctive of FHF cells (**Figure 13 A**). TBX5, a specific marker of FHF, was mainly found in ISL1^{low}/NKX2-5^{high} cells (**Figure 13 A**), confirming FHF identity. Notably, the relative distribution of the CP subgroups was altered in HLHS settings: HLHS1 and HLHS3 lines showed an increase of early committed (ISL1^{low}/NKX2-5^{low}) CPs at the expense of the fully committed (ISL1^{high}/NKX2-5^{high}) and SHF (ISL1^{high}/NKX2-5^{low}) populations, while line HLHS2 exhibited a higher proportion of FHF (ISL1^{low}/NKX2-5^{high}) cells (**Figure 13 B**).

Importantly, all HLHS lines failed to upregulate TBX5 transcript during CP differentiation (**Figure 12 A**) and only few of the ISL1low/NKX2-5high FHF cells expressed TBX5 protein (**Figure 13 C**), indicating common defective transcriptional programs within the FHF lineage.

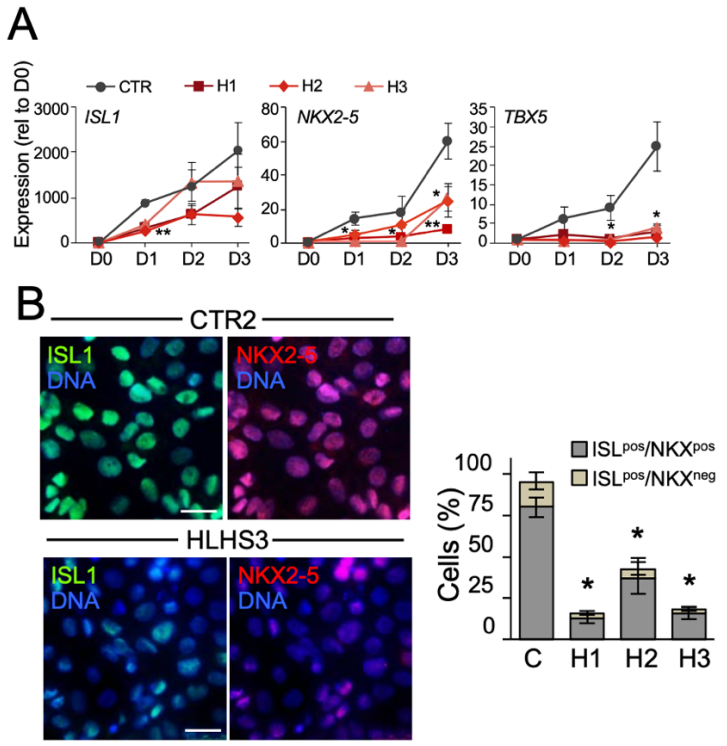

Figure 12. CP markers expression at mRNA and protein level in HLHS lines. (A) Time-course qRT-PCR analysis of ISL1, NKX2-5 and TBX5 during CP differentiation of HLHS and control hiPSCs. Data are mean ± SEM, n=3-6 differentiations per line. *p<0.05, **p<0.01 (t test). (B) Immunofluorescence analysis of ISL1 and NKX2-5 in HLHS and control CPs at D2. Scale bar, 25 µm. Data are mean ± SEM, n=3 differentiations per line. *p<0.05 (t test).

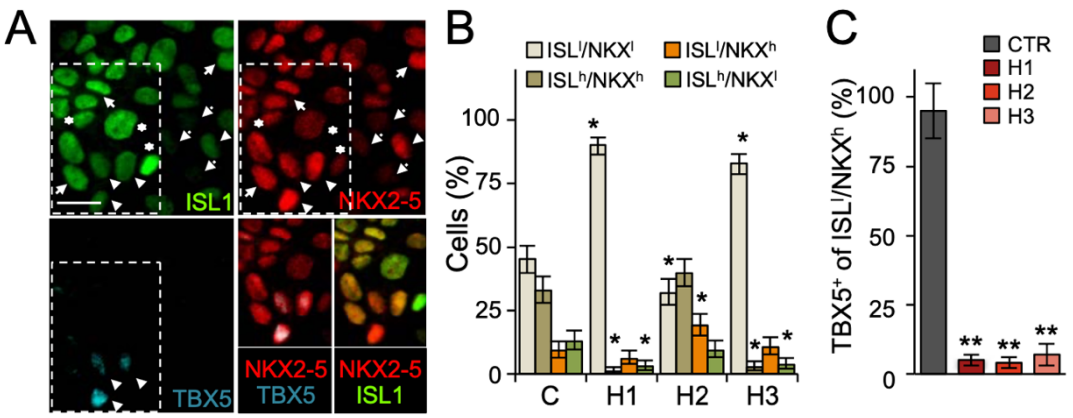

Figure 13. Quantification of CP markers expression in HLHS lines. (A) Representative immunofluorescence of ISL1, NKX2-5 and TBX5 in control CPs (CTR3) at D3. Four ISL1/NKX2-5 expression patterns are highlighted: ISL1^{low}/NKX2-5^{low} (dotted arrows), ISL1^{high}/NKX2-5^{high} (arrows), ISL1^{high}/NKX2-5^{low} (asterisks), and ISL1^{low}/NKX2-5^{high} (arrow heads). Scale bar, 20 µm. (B) Distribution of cells with

ISL1/NKX2-5 expression patterns from (A) in HLHS and control CPs at D3. Data are mean ± 95% CI, n>320 cells from 3 differentiations per line. *p<0.05 (t test). (C) Percentage of ISL1low/NKX2-5high cells expressing TBX5 in HLHS and control CPs at D3. Data are mean ± SEM, n=3 differentiations per line. **p<0.005 (t test).

3.3 Proliferation and apoptosis in HLHS CPs

To assess the contribution of apoptosis/proliferation to the observed CP phenotypes, we analysed activation of caspase 3 and EdU incorporation during CP specification. Apoptosis was barely detectable during the entire time course, with no differences between HLHS and controls (**Figure 14 A**), arguing against any cell selection of HLHS CPs. Consistent with the alteration in cell cycle patterns, global changes in cell proliferation rates between control and HLHS cells were only significantly different at D2 (**Figure 14 B**). However, when analyzed separately at D3, ISL1^{low}/NKX2-5^{high} FHF progenitors demonstrated higher proliferation in all HLHS lines (**Figure 14 C**), consistent with the reported role of TBX5 as negative regulator of cell proliferation during early cardiac development (Hatcher CJ. et al., 2001). Collectively, these data indicate common defects in CP lineage commitment and imbalance of the two progenitor fields during the initial steps of HLHS cardiogenesis. Moreover, they reveal intrinsic molecular and functional abnormalities in FHF progenitors, with impaired TBX5 upregulation and enhanced cell proliferation.

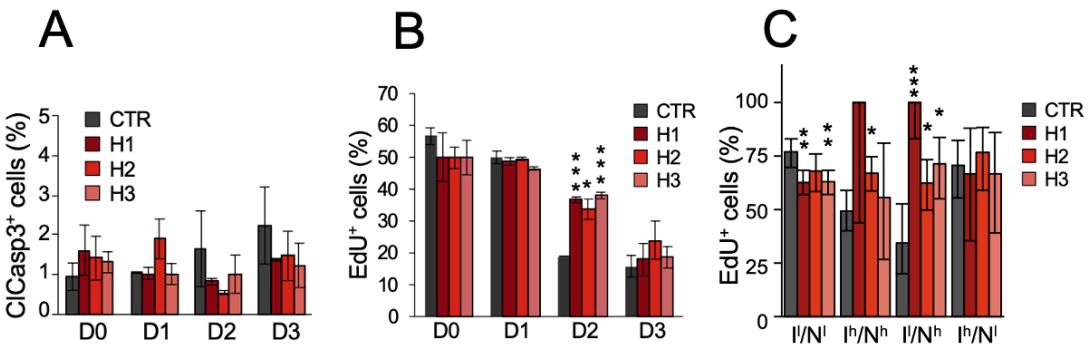

Figure 14. Proliferation and apoptosis quantification in HLHS lines. (A) Time-course immunostaining quantification of activated caspase-3 (ClCasp3) in HLHS and control cells. Data are mean ± SEM, n=3 differentiations per line. (B) Flow-cytometry quantification of EdU+ cells in HLHS and control cells during CP differentiation. Data are mean ± SEM, n=3 differentiations per line. *p<0.05, ***p<0.001 (t test). (C) Quantification of EdU+ cells in HLHS and control CP subpopulations at D3. Data are mean ± 95% CI, n>320 cells from 3 differentiations per line. *p<0.05, **p<0.005, ***p<0.001 (t test).

3.4 Primary cilia in HLHS CPs

Ciliogenesis is tightly linked to cell cycle progression, with primary cilium assembly occurring in G1 phase and disassembly in G2 phase (Plotnikova OV. et al., 2009). In M phase, cilia are absent, and their basal body participates as the centrosome of the mitotic-spindle (Santos N and Reiter JF, 2008). A key role of the primary cilium in neuroectodermal versus mesendodermal cell fate decisions has been described (Jang J. et al., 2016).

To test whether the alterations in cell cycle progression and CP lineage commitment associated with ciliogenesis defects, we analysed the number of ciliated cells and cilia length in CPs at D2 of differentiation before bifurcation of FHF/SHF fates occurred and when differences in G1 length (**Figure 11 B**) and upregulation of cilium-related pathways (**Figure 8 B**) were detected. Immunocytochemistry for the ciliary axoneme marker acetylated a-tubulin and the basal body protein pericentrin demonstrated an abnormal percentage of ciliated cells in HLHS CPs; interestingly, HLHS1 and HLHS2 lines had more ciliated cells when compared to controls, while HLHS3 had less (**Figure 15**). Defective cilia length was also appreciated in all HLHS lines (**Figure 15**).

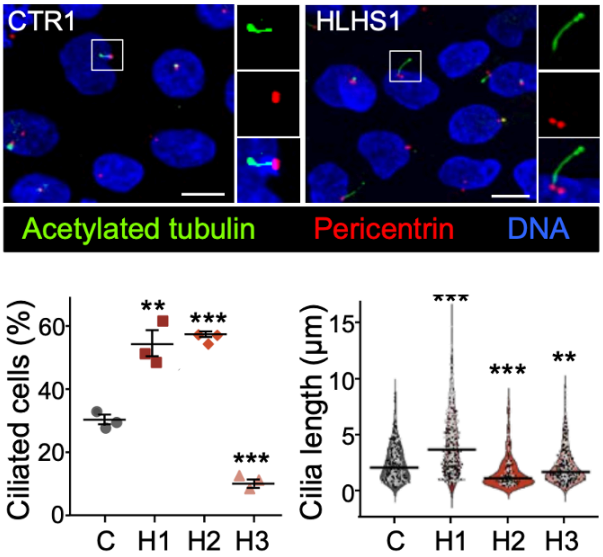

Figure 15. Structural cilia alterations in HLHS lines. Upper panel: Immunostaining for acetylated tubulin and pericentrin in HLHS and control CPs at D2. Scale bar, 10 µm. Lower panel: Dot plot graph summarizes the percentage of ciliated cells in each line. Violin plot graph shows the distribution of cilia

length. Data are mean ± SEM, n=3differentiations per line. **p<0.01, ***p<0.001 (t test and Wilcoxon test for cilia frequency and length, respectively).

Expression of key structural and functional cilia genes correlated with the observed structural phenotypic alterations (**Figure 16 A**). We further analyzed the Hedgehog/Smoothened signalling as one of the main pathways transduced by cilia (Rohatgi R. et al., 2007), which was highly enriched for D-DNMs in our HLHS cohort. Genes required for Hedgehog response were likewise dysregulated in HLHS CPs consistently with the cilia phenotype, including SMO and the downstream targets GLI1, and PTCH1 (**Figures 16 A and B**). However, pharmacological activation (SAG) or repression (cyclopamine) of Smoothened in D2 CPs was insufficient to rescue the impaired TBX5 upregulation shared by all HLHS CPs and, importantly, did not alter TBX5 expression in control CPs (**Figure 16 C**), suggesting that this pathway has little impact on early FHF CP development.

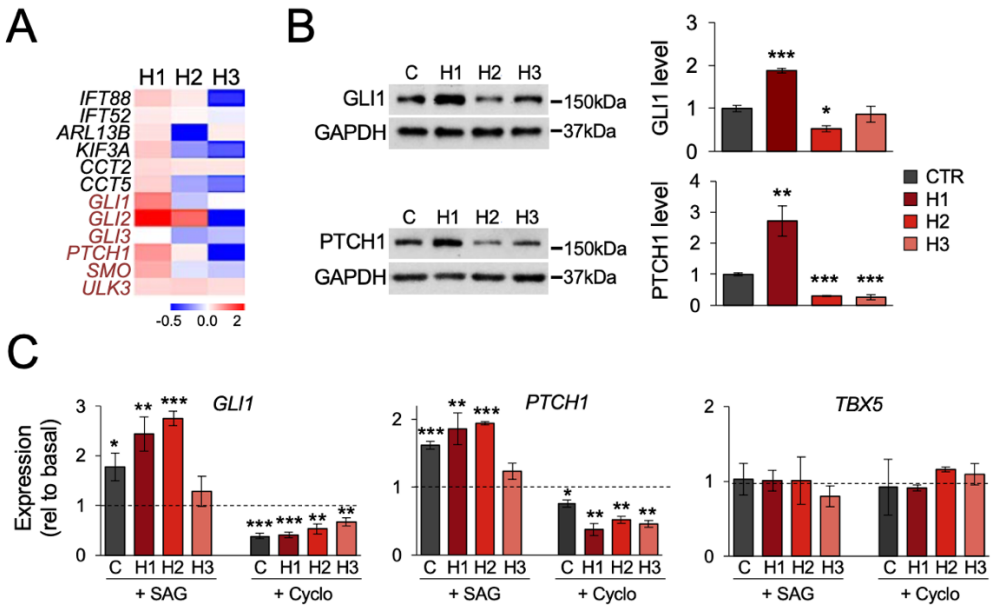

Figure 16. Functional cilia alterations in HLHS lines. (A) Heatmap showing expression level of genes involved in ciliogenesis (black) and Smoothened pathway (red) in HLHS and control CPs at D2. Data are log2 mean fold changes relative to controls, n=3 differentiations per line. (B) Western blot of GLI1 and PTCH1 in HLHS and control CPs at D2. Data are mean ± SEM, n=2-4 differentiations per line. *p<0.05, **p<0.005, ***p<0.001 (t test). (C) Quantitative RT-PCR analysis of GLI1, PTCH1, and TBX5 in HLHS and control CPs after a 24h-treatment with the Smoothened activator SAG (1 μM) or the Smoothened inhibitor cyclopamine (15 μM). GLI1, PTCH1 and TBX5 levels were measured at D2 and

D3, respectively. Data are mean ± SEM, n=3 differentiations per line. *p<0.05, **p<0.01, ***p<0.001 (t test).

3.5 Autophagy in HLHS CPs

Several studies have demonstrated a tight interplay between cilia and autophagy. Signaling from the primary cilium recruits the autophagic machinery to trigger autophagosome formation (Pampliega O. et al., 2013). Conversely, autophagy regulates ciliogenesis by controlling the levels of ciliary proteins (Pampliega O. and Cuervo AM., 2016, 2016). Notably, blockage of autophagy can either increase or decrease ciliary length dependently on the selective degradation of proteins that contribute to ciliary growth or block ciliogenesis (Pampliega O. and Cuervo AM., 2016). Since autophagy was downregulated in HLHS CPs from D1 on (**Figure 8 B**), we measured autophagic flux in cells at D3 by analyzing the protein levels of LC3II, a marker of autophagosomes, and p62, a substrate for autophagic degradation. Under basal conditions, LC3II and p62 levels were normal in all HLHS lines, as assessed by western blot (**Figure 17 A**) and immunofluorescence analysis (**Figure 17 B**). However, after activation of autophagy either by starvation or with brefeldin A, we measured defective autophagosome formation and p62 degradation, which was common to all HLHS lines (**Figure 17 A**). This was also confirmed by Cyto-ID staining of autophagic vacuoles (**Figure 17 C**).

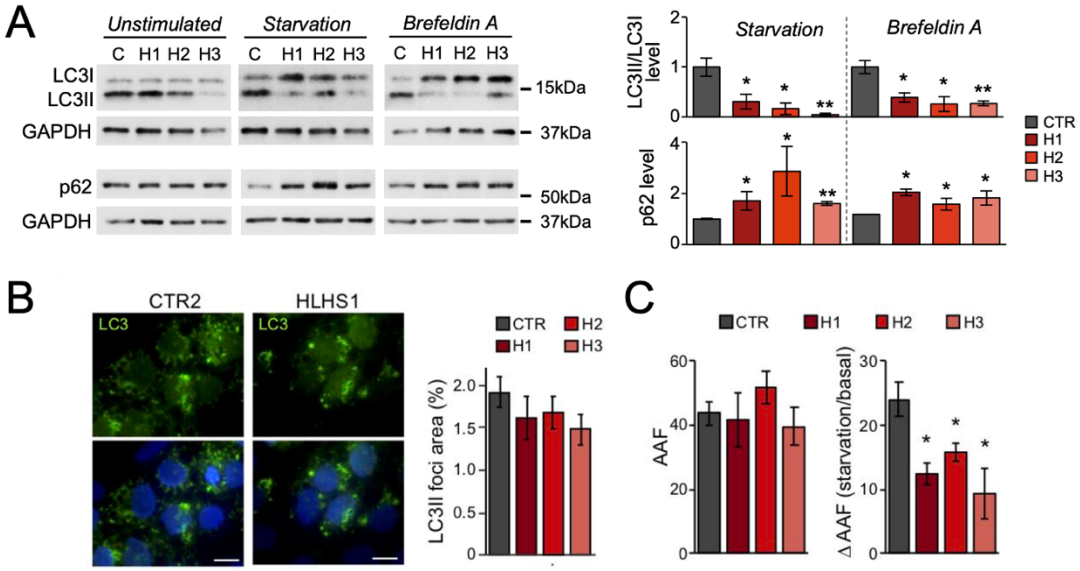

Figure 17. Autophagy analyses in HLHS lines. (A) Western blot of LC3 and p62 in HLHS and control CPs at D3 with and without starvation or brefeldin A. For detection of LC3, all three conditions were carried out in presence of chloroquine. Data are mean ± SEM, n=2-3 differentiations per line. *p<0.05, **p<0.01 (t test). (B) Immunofluorescence analysis of LC3II foci in HLHS and control CPs at D3. Scale bar, 5 μm. Data are mean ± SEM, n=30 cells from 3 independent differentiations per line. (C) FACS-based quantification of the autophagy activity factor (AAF) in HLHS and control CPs at D3 by autophagic vesicle labeling with CYTO-ID. Data are mean ± SEM, n=3 differentiations per line. *p<0.05 (t test).

3.6 Unfolded protein response in HLHS CPs

Brefeldin A is an inhibitor of protein transport between ER and Golgi (Donaldson JG. et al., 1992) and triggers autophagy via ER stress and activation of the unfolded protein response (UPR), a pathway also challenged by starvation. As surveillance mechanism of protein homeostasis, UPR plays an important role in lineage differentiation of embryonic and adult stem cells, partially by impacting cell cycle progression (Heijmans J. et al., 2013; Xu H. et al., 2014) and has been reported to control cell fate acquisition of neuronal progenitors during cortical neurogenesis (Laguesse S. et al., 2015). Moreover, evidence exist that UPR is critical during the early stages of cardiogenesis (Mao C. et al., 2006; Masaki T. et al., 1999). Given the recovery of D-DNMs in ER-stress/UPR genes in our HLHS cohort we asked whether the observed defects of HLHS CPs in activating autophagy could be due to impaired UPR. Upon ER stress, UPR is transduced by de-repression of three integral ER membrane proteins, IRE1α (inositol-requiring enzyme1α), PERK (double-stranded RNA-dependent protein kinase-like ER kinase), and ATF6 (activating transcription factor 6) that work alone or in concert to restore normal cellular function by controlling protein translation, folding, and degradation (Hetz C., 2012). Interestingly, neither an increased splicing of XBP1 mRNA, which occurs downstream of IRE1α stimulation, nor the activation of ATF6 were altered in HLHS CPs at D3 upon brefeldin A treatment (**Figure 18 A**). Instead, we measured a specific common defect of all HLHS lines in activating the PERK pathway, as indicated by decreased PERK-mediated phosphorylation of the eukaryotic translation initiation factor 2 α (eIF2α) (**Figure 18 B**) and reduced increase of ATF4 and its downstream targets ATG3, ATG5, ATG12, and CHOP (**Figures 18 C and 18 A**).

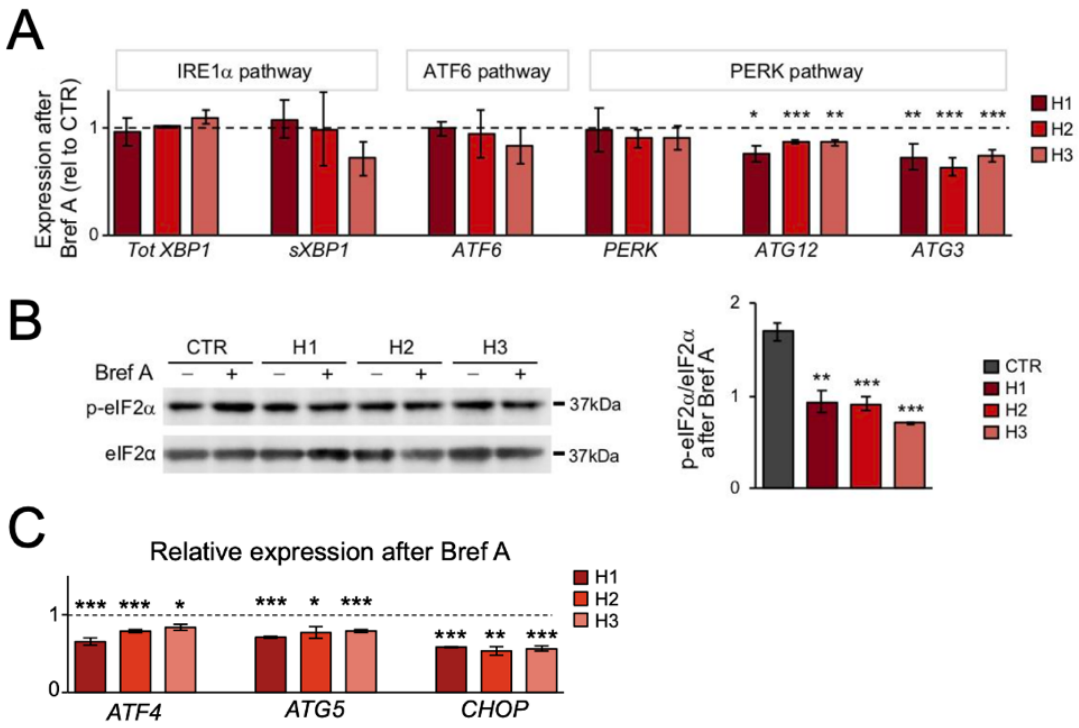

Figure 18. Unfolded protein response in HLHS lines. (A) Expression levels of UPR actors in HLHS and control CPs at D3 after brefeldin A treatment. Data are mean ± SEM, n=3 differentiations per line. *p<0.05, **p<0.005, ***p<0.001 (t test). (B) Western blot of total and phosphorylated eIF2α (eIF2α and p-eIF2α) in HLHS and control CPs at D3 with or without brefeldin A. Data are mean ± SEM, n=3 differentiations per line. **p<0.01, ***p<0.001 (t test). (C) Expression analysis of ATF4 and its downstream targets in HLHS and control CPs at D3 after treatment with brefeldin A.

A six-hour treatment of HLHS cells with the selective PERK activator CCT020312 normalized ATF4 and CHOP levels after brefeldin A and rescued the defective activation of autophagy (**Figures 19 A and B**). Importantly, early application of CCT020312 at D1.5 of CP differentiation was sufficient to revert aspects of the HLHS phenotype, as indicated by normalization of the number of cells in G1 at D2 as well as the level of TBX5 at D3 (**Figure 19 C**). Conversely, HLHS-like disturbances in G1-phase lengthening and TBX5 upregulation could be induced in control cells by inhibiting autophagy at D1.5 using chloroquine, with no influence on ISL1 expression (**Figure 19 D**).

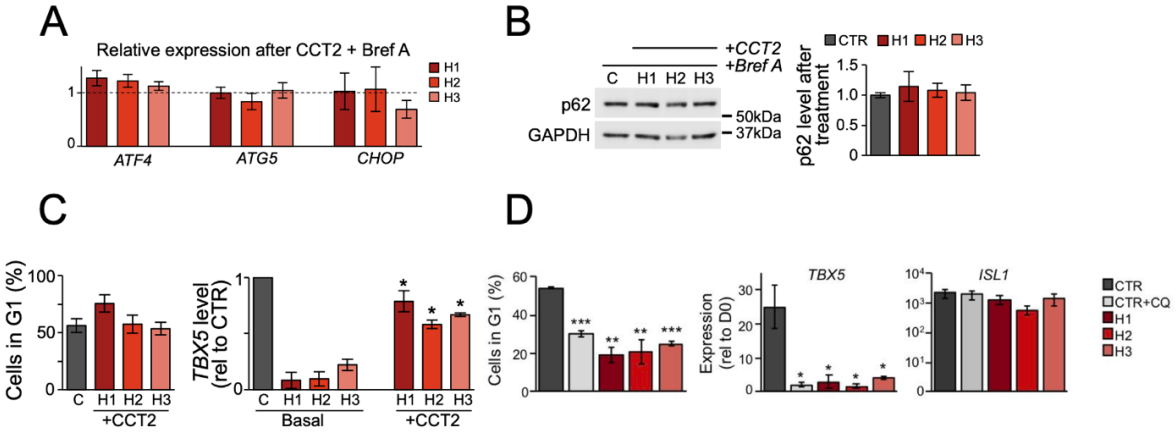

Figure 19. Modulation of unfolded protein response and autophagy in HLHS lines. (A) Expression analysis of ATF4 and its downstream targets in HLHS and control CPs at D3 after treatment with brefeldin A with the PERK activator CCT020312 Shown are expression levels relative to controls. Data are mean ± SEM, n=3 differentiations per line. *p<0.05, **p<0.005, ***p<0.001 (t test). (B) Western blot of p62 in HLHS and control CPs at D3 after treatment with brefeldin A and CCT020312. Data are mean ± SEM, n=3 differentiations per line. (C) Propidium iodide staining-based quantification of cells in G1 phase in HLHS and control CPs at D2 (left) and TBX5 expression by qRT-PCR at D3 (right) after 6h-treatment of HLHS cells with CCT020312 at D1.5. Data are mean ± SEM, n=3 differentiations per line. *p<0.05 compared to own basal (t test). (D) Analysis of 12-hour chloroquine (CQ) treatment in control CPs. Left bar graph shows propidium iodide staining-based quantification of cells in G1 phase in HLHS and control CPs at D2 with or without chloroquine. Middle and right bar graphs summarize qRT-PCR analysis of TBX5 and ISL1 expression, respectively, in control CPs (with or without chloroquine) and in HLHS CPs at D3. Data are mean ± SEM, n=3 differentiations per line. *p<0.05, **p<0.01, ***p<0.001 (t test).

Taken together, these results suggest that defects in UPR and autophagy activation in the early phase of CP specification contribute to delayed CP formation and disrupted CP lineage commitment in HLHS pathology.

4. Discussion

Our study provides robust evaluation of the transcriptional and cellular perturbations observed during progression of cardiogenesis in HLHS patients, offering the opportunity to identify new targets for mechanism-based therapy. Study of patient-derived hiPSC-cardiac lineages allowed the possibility to dynamically evaluate new transcriptional and cellular phenotypes, that were not described in advance.

Together, our data indicate that our data indicate that initial perturbations of the cell cycle-ciliogenesis-UPR/autophagy hub result in disrupted differentiation of early FHF/SHF CP lineages and disproportionate allocation of ventricular CM subtypes in HLHS.

4.1 Identification of dysregulated transcriptional and cellular nodes

We systematically interrogated the transcriptional consequences of the complex genetic landscape of HLHS through genome-wide transcriptomics of hiPSC-derived cardiac lineages during normal and diseased human cardiac development. We identified dysregulated transcriptional nodes that were common in both CP and CM states (e.g., those centered on heart development, cell cycle, and chromatin modification) or unique of specific developmental cellular stages (e.g., cilium/autophagy for CPs and apoptosis for CMs).

Other groups have reported transcriptional repression of specific cardiac genes such as NKX2-5, HAND1 and NOTCH1 in HLHS iPSC differentiated CMs (Kobayashi J. et al., 2014) and reduced cardiac differentiation potential as well as structural CM maturation in presence of dysfunctional NOTCH signaling (Hrstka SC. et al., 2017; Theis JL. et al., 2015; Yang C. et al., 2017).

Moreover, based on the expression of specific cardiac markers during iPSC differentiation, a previous study suggested defective commitment to the ventricular lineage in HLHS (Jiang Y. et al., 2014).

By corroborating these previous works, our iPSC-based modeling identifies key sequential molecular and cellular mechanisms leading to the observed HLHS phenotypes. Aberrations in the cell cycle/cilium/autophagy-UPR hub are evident during early CP commitment and result in disrupted FHF/SHF development and ultimately defective CM-subtype differentiation/maturation.

Importantly, evidence of cell cycle arrest and impaired growth/maturation has been reported in ventricular CMs of the Ohia HLHS mouse model (Liu X. et al., 2017) and LV of patient fetuses (Gaber N. et al., 2013). Loss of replication potential during the critical fetal growth phase is likely to impair cardiac chamber development and function. One reason why cell cycle perturbation and loss of CM proliferation in HLHS may affect more dramatically LV than RV development could rely on the differences in proliferation rates that exist between LV and RV CMs at very early stages of heart chamber formation. By analyzing the cell cycle gene signature of single CMs from RV and LV regions of human embryonic hearts from 5 to 25 weeks of gestation (Cui Y. et al., 2019), we found that LV CMs seem more actively proliferating than their RV counterpart at 5 weeks (58% LV vs 48% RV), but these differences are abolished later in development (45% and 55% LV vs 43% and 53% RV at 6 and 7 weeks, respectively).

4.2 Linking clinical phenotype to mechanism and concluding remarks

HLHS is a spectrum of disease that includes LV and aortic hypoplasia with aortic and mitral valve malformations ranging from stenosis to complete atresia. Clinically, a generally accepted (though experimentally sparsely supported in mammals) mechanistic hypothesis is “no flow, no growth” (Harh JY. et al, 1973; Hogers B. et al., 1997). However, recent observations in patients (Crucean A. et al., 2017) and in the Ohia HLHS mouse model (Liu X. et al., 2017) argue for an uncoupling of the hemodynamic conditions and the resulting LV size. In our study we were able to identify a common mechanism for the development of the hypoplastic LV with a distinct morphology. These findings may have a direct clinical impact on stratification and treatment strategies for children with HLHS. During the last decade intrauterine, fetal valvuloplasty in HLHS patients has been proposed as treatment option to enable LV growth. However, the existence of intrinsic CP and CM defects suggest a mechanism to

explain the ineffectiveness of a 10-year, in utero aortic valvuloplasty clinical trial (Freud et al., 2014).

Taken together, our results suggest that a shared mechanism might exist for HLHS. Moreover, they highlight that reduced LV growth in HLHS is likely not a sole consequence of disrupted valve formation and impaired blood flow, but a primary, intrinsic defect of ventricular CP/CM lineage specification and development.

More broadly, our work illustrates that, despite the extensive genetic heterogeneity underlying CHD, studying cardiac developmental processes in CHD patients using converging multidimensional technologies can provide deep mechanistic insight into these complex diseases and suggest novel therapeutic approaches.

5. References

Ang YS, Rivas RN, Ribeiro AJS, et al. Disease Model of GATA4 Mutation Reveals Transcription Factor Cooperativity in Human Cardiogenesis. Cell. 2016;167(7):1734-1749.e22. doi:10.1016/j.cell.2016.11.033

Bruneau BG, Logan M, Davis N, et al. Chamber-specific cardiac expression of Tbx5 and heart defects in Holt-Oram syndrome. Dev Biol. 1999;211(1):100-108. doi:10.1006/dbio.1999.9298

Bruneau BG, Nemer G, Schmitt JP, et al. A murine model of Holt-Oram syndrome defines roles of the T-box transcription factor Tbx5 in cardiogenesis and disease. Cell. 2001;106(6):709-721. doi:10.1016/s0092-8674(01)00493-7

Bruneau BG. The developmental genetics of congenital heart disease. Nature. 2008;451(7181):943-948. doi:10.1038/nature06801

Burridge PW, Matsa E, Shukla P, et al. Chemically defined generation of human cardiomyocytes. Nat Methods. 2014;11(8):855-860. doi:10.1038/nmeth.2999

Cao N, Liang H, Huang J, et al. Highly efficient induction and long-term maintenance of multipotent cardiovascular progenitors from human pluripotent stem cells under defined conditions. Cell Res. 2013;23(9):1119-1132. doi:10.1038/cr.2013.102

Chan LL, Shen D, Wilkinson AR, et al. A novel image-based cytometry method for autophagy detection in living cells. Autophagy. 2012;8(9):1371-1382. doi:10.4161/auto.21028

Chu CT, Plowey ED, Dagda RK, Hickey RW, Cherra SJ 3rd, Clark RS. Autophagy in neurite injury and neurodegeneration: in vitro and in vivo models. Methods Enzymol. 2009;453:217-249. doi:10.1016/S0076-6879(08)04011-1

Crucean A, Alqahtani A, Barron DJ, et al. Re-evaluation of hypoplastic left heart syndrome from a developmental and morphological perspective. Orphanet J Rare Dis. 2017;12(1):138. Published 2017 Aug 10. doi:10.1186/s13023-017-0683-4

Cui Y, Zheng Y, Liu X, et al. Single-Cell Transcriptome Analysis Maps the Developmental Track of the Human Heart. Cell Rep. 2019;26(7):1934-1950.e5. doi:10.1016/j.celrep.2019.01.079

Dagda RK, Zhu J, Kulich SM, Chu CT. Mitochondrially localized ERK2 regulates mitophagy and autophagic cell stress: implications for Parkinson's disease. Autophagy. 2008;4(6):770-782. doi:10.4161/auto.6458

Donaldson JG, Finazzi D, Klausner RD. Brefeldin A inhibits Golgi membrane-catalysed exchange of guanine nucleotide onto ARF protein. Nature. 1992;360(6402):350-352. doi:10.1038/360350a0

Dorn T, Goedel A, Lam JT, et al. Direct nkx2-5 transcriptional repression of isl1 controls cardiomyocyte subtype identity. Stem Cells. 2015;33(4):1113-1129. doi:10.1002/stem.1923

Freud LR, McElhinney DB, Marshall AC, et al. Fetal aortic valvuloplasty for evolving hypoplastic left heart syndrome: postnatal outcomes of the first 100 patients. Circulation. 2014;130(8):638-645. doi:10.1161/CIRCULATIONAHA.114.009032

Gaber N, Gagliardi M, Patel P, et al. Fetal reprogramming and senescence in hypoplastic left heart syndrome and in human pluripotent stem cells during cardiac differentiation. Am J Pathol. 2013;183(3):720-734. doi:10.1016/j.ajpath.2013.05.022

Gramlich M, Pane LS, Zhou Q, et al. Antisense-mediated exon skipping: a therapeutic strategy for titin-based dilated cardiomyopathy. EMBO Mol Med. 2015;7(5):562-576. doi:10.15252/emmm.201505047

Harh JY, Paul MH, Gallen WJ, Friedberg DZ, Kaplan S. Experimental production of hypoplastic left heart syndrome in the chick embryo. Am J Cardiol. 1973;31(1):51-56. doi:10.1016/0002-9149(73)90810-2

Hatcher CJ, Kim MS, Mah CS, et al. TBX5 transcription factor regulates cell proliferation during cardiogenesis. Dev Biol. 2001;230(2):177-188. doi:10.1006/dbio.2000.0134

Heijmans J, van Lidth de Jeude JF, Koo BK, et al. ER stress causes rapid loss of intestinal epithelial stemness through activation of the unfolded protein response. Cell Rep. 2013;3(4):1128-1139. doi:10.1016/j.celrep.2013.02.031

Hetz C. The unfolded protein response: controlling cell fate decisions under ER stress and beyond. Nat Rev Mol Cell Biol. 2012;13(2):89-102. Published 2012 Jan 18. doi:10.1038/nrm3270

Hickey EJ, Caldarone CA, McCrindle BW. Left ventricular hypoplasia: a spectrum of disease involving the left ventricular outflow tract, aortic valve, and aorta. J Am Coll Cardiol. 2012;59(1 Suppl):S43-S54. doi:10.1016/j.jacc.2011.04.046

Hinton RB Jr, Martin LJ, Tabangin ME, Mazwi ML, Cripe LH, Benson DW. Hypoplastic left heart syndrome is heritable. J Am Coll Cardiol. 2007;50(16):1590-1595. doi:10.1016/j.jacc.2007.07.021

Hoffman JI, Kaplan S. The incidence of congenital heart disease. J Am Coll Cardiol. 2002;39(12):1890-1900. doi:10.1016/s0735-1097(02)01886-7

Hogers B, DeRuiter MC, Gittenberger-de Groot AC, Poelmann RE. Unilateral vitelline vein ligation alters intracardiac blood flow patterns and morphogenesis in the chick embryo. Circ Res. 1997;80(4):473-481. doi:10.1161/01.res.80.4.473

Hrstka SC, Li X, Nelson TJ; Wanek Program Genetics Pipeline Group. NOTCH1-Dependent Nitric Oxide Signaling Deficiency in Hypoplastic Left Heart Syndrome Revealed Through Patient-Specific Phenotypes Detected in Bioengineered Cardiogenesis. Stem Cells. 2017;35(4):1106-1119. doi:10.1002/stem.2582

Ikenishi A, Okayama H, Iwamoto N, et al. Cell cycle regulation in mouse heart during embryonic and postnatal stages. Dev Growth Differ. 2012;54(8):731-738. doi:10.1111/j.1440-169X.2012.01373.x

Jain R, Epstein JA. Competent for commitment: you've got to have heart!. Genes Dev. 2018;32(1):4-13. doi:10.1101/gad.308353.117

Jang J, Wang Y, Lalli MA, et al. Primary Cilium-Autophagy-Nrf2 (PAN) Axis Activation Commits Human Embryonic Stem Cells to a Neuroectoderm Fate. Cell. 2016;165(2):410-420. doi:10.1016/j.cell.2016.02.014

Jiang Y, Habibollah S, Tilgner K, et al. An induced pluripotent stem cell model of hypoplastic left heart syndrome (HLHS) reveals multiple expression and functional differences in HLHS-derived cardiac myocytes. Stem Cells Transl Med. 2014;3(4):416-423. doi:10.5966/sctm.2013-0105

Kattman SJ, Huber TL, Keller GM. Multipotent flk-1+ cardiovascular progenitor cells give rise to the cardiomyocyte, endothelial, and vascular smooth muscle lineages. Dev Cell. 2006;11(5):723-732. doi:10.1016/j.devcel.2006.10.002

Kobayashi J, Yoshida M, Tarui S, et al. Directed differentiation of patient-specific induced pluripotent stem cells identifies the transcriptional repression and epigenetic modification of NKX2-5, HAND1, and NOTCH1 in hypoplastic left heart syndrome. PLoS One. 2014;9(7):e102796. Published 2014 Jul 22. doi:10.1371/journal.pone.0102796

Kodo K, Ong SG, Jahanbani F, et al. iPSC-derived cardiomyocytes reveal abnormal TGF-β signalling in left ventricular non-compaction cardiomyopathy. Nat Cell Biol. 2016;18(10):1031-1042. doi:10.1038/ncb3411

Laguesse S, Creppe C, Nedialkova DD, et al. A Dynamic Unfolded Protein Response Contributes to the Control of Cortical Neurogenesis. Dev Cell. 2015;35(5):553-567. doi:10.1016/j.devcel.2015.11.005

Lange C, Calegari F. Cdks and cyclins link G1 length and differentiation of embryonic, neural and hematopoietic stem cells. Cell Cycle. 2010;9(10):1893-1900. doi:10.4161/cc.9.10.11598

Laugwitz KL, Moretti A, Caron L, Nakano A, Chien KR. Islet1 cardiovascular progenitors: a single source for heart lineages? Development. 2008;135(2):193-205. doi:10.1242/dev.001883

Lee JH, Protze SI, Laksman Z, Backx PH, Keller GM. Human Pluripotent Stem Cell-Derived Atrial and Ventricular Cardiomyocytes Develop from Distinct Mesoderm Populations. Cell Stem Cell. 2017;21(2):179-194.e4. doi:10.1016/j.stem.2017.07.003

Lescroart F, Wang X, Lin X, et al. Defining the earliest step of cardiovascular lineage segregation by single-cell RNA-seq. Science. 2018;359(6380):1177-1181. doi:10.1126/science.aao4174

Lev M. Pathologic anatomy and interrelationship of hypoplasia of the aortic tract complexes. Lab Invest. 1952;1(1):61-70.

Li Y, Klena NT, Gabriel GC, et al. Global genetic analysis in mice unveils central role for cilia in congenital heart disease. Nature. 2015;521(7553):520-524. doi:10.1038/nature14269

Liu X, Yagi H, Saeed S, et al. The complex genetics of hypoplastic left heart syndrome. Nat Genet. 2017;49(7):1152-1159. doi:10.1038/ng.3870

Mao C, Tai WC, Bai Y, Poizat C, Lee AS. In vivo regulation of Grp78/BiP transcription in the embryonic heart: role of the endoplasmic reticulum stress response element and GATA-4. J Biol Chem. 2006;281(13):8877-8887. doi:10.1074/jbc.M505784200

Masaki T, Yoshida M, Noguchi S. Targeted disruption of CRE-binding factor TREB5 gene leads to cellular necrosis in cardiac myocytes at the embryonic stage. Biochem Biophys Res Commun. 1999;261(2):350-356. doi:10.1006/bbrc.1999.0972

Meilhac SM, Lescroart F, Blanpain C, Buckingham ME. Cardiac cell lineages that form the heart [published correction appears in Cold Spring Harb Perspect Med. 2015 Feb;5(2):a026344] [published correction appears in Cold Spring Harb Perspect Med. 2015 Feb;5(2):a026344]. Cold Spring Harb Perspect Med. 2014;4(9):a013888. Published 2014 Sep 2. doi:10.1101/cshperspect.a013888

Misra C, Chang SW, Basu M, Huang N, Garg V. Disruption of myocardial Gata4 and Tbx5 results in defects in cardiomyocyte proliferation and atrioventricular septation. Hum Mol Genet. 2014;23(19):5025-5035. doi:10.1093/hmg/ddu215

Moretti A, Caron L, Nakano A, et al. Multipotent embryonic isl1+ progenitor cells lead to cardiac, smooth muscle, and endothelial cell diversification. Cell. 2006;127(6):1151-1165. doi:10.1016/j.cell.2006.10.029

Moretti, A., Bellin, M., Welling, A., Jung, C.B., Lam, J.T., Bott-Flugel, L., Dorn, T., Goedel, A., Hohnke, C., Hofmann, F., et al. 2010. Patient-specific induced pluripotent stem-cell models for long-QT syndrome. N Engl J Med 363, 1397-1409.

Moretti A, Fonteyne L, Giesert F, et al. Somatic gene editing ameliorates skeletal and cardiac muscle failure in pig and human models of Duchenne muscular dystrophy. Nat Med. 2020;26(2):207-214. doi:10.1038/s41591-019-0738-2

Noonan JA, Nadas AS. The hypoplastic left heart syndrome; an analysis of 101 cases. Pediatr Clin North Am. 1958;5(4):1029-1056. doi:10.1016/s0031-3955(16)30727-1

Øyen N, Poulsen G, Boyd HA, Wohlfahrt J, Jensen PK, Melbye M. Recurrence of congenital heart defects in families. Circulation. 2009;120(4):295-301. doi:10.1161/CIRCULATIONAHA.109.857987

Pane LS., My I., Moretti A. Induced Pluripotent Stem Cells in Regenerative Medicine, Regenerative Medicine - from Protocol to Patient pp 51-75., Springer 2016.

Pampliega O, Cuervo AM. Autophagy and primary cilia: dual interplay. Curr Opin Cell Biol. 2016;39:1-7. doi:10.1016/j.ceb.2016.01.008

Pampliega O, Orhon I, Patel B, et al. Functional interaction between autophagy and ciliogenesis. Nature. 2013;502(7470):194-200. doi:10.1038/nature12639

Pauklin S, Vallier L. The cell-cycle state of stem cells determines cell fate propensity [published correction appears in Cell. 2014 Mar 13;156(6):1338]. Cell. 2013;155(1):135-147. doi:10.1016/j.cell.2013.08.031

Plotnikova OV, Pugacheva EN, Golemis EA. Primary cilia and the cell cycle. Methods Cell Biol. 2009;94:137-160. doi:10.1016/S0091-679X(08)94007-3

Preuss C, Capredon M, Wünnemann F, et al. Family Based Whole Exome Sequencing Reveals the Multifaceted Role of Notch Signaling in Congenital Heart Disease. PLoS Genet. 2016;12(10):e1006335. Published 2016 Oct 19. doi:10.1371/journal.pgen.1006335

Protze SI, Liu J, Nussinovitch U, et al. Sinoatrial node cardiomyocytes derived from human pluripotent cells function as a biological pacemaker. Nat Biotechnol. 2017;35(1):56-68. doi:10.1038/nbt.3745

Rohatgi R, Milenkovic L, Scott MP. Patched1 regulates hedgehog signaling at the primary cilium. Science. 2007;317(5836):372-376. doi:10.1126/science.1139740

Santos N, Reiter JF. Building it up and taking it down: the regulation of vertebrate ciliogenesis. Dev Dyn. 2008;237(8):1972-1981. doi:10.1002/dvdy.21540

Takahashi K, Yamanaka S. Induction of pluripotent stem cells from mouse embryonic and adult fibroblast cultures by defined factors. Cell. 2006;126(4):663-676. doi:10.1016/j.cell.2006.07.024

Takeuchi JK, Mileikovskaia M, Koshiba-Takeuchi K, et al. Tbx20 dose-dependently regulates transcription factor networks required for mouse heart and motoneuron development. Development. 2005;132(10):2463-2474. doi:10.1242/dev.01827

Theis JL, Hrstka SC, Evans JM, et al. Compound heterozygous NOTCH1 mutations underlie impaired cardiogenesis in a patient with hypoplastic left heart syndrome. Hum Genet. 2015;134(9):1003-1011. doi:10.1007/s00439-015-1582-1

White J, Dalton S. Cell cycle control of embryonic stem cells. Stem Cell Rev. 2005;1(2):131-138. doi:10.1385/SCR:1:2:131

Xu H, Tsang KS, Wang Y, Chan JC, Xu G, Gao WQ. Unfolded protein response is required for the definitive endodermal specification of mouse embryonic stem cells via Smad2 and β-catenin signaling. J Biol Chem. 2014;289(38):26290-26301. doi:10.1074/jbc.M114.572560

Yang C, Xu Y, Yu M, et al. Induced pluripotent stem cell modelling of HLHS underlines the contribution of dysfunctional NOTCH signalling to impaired cardiogenesis. Hum Mol Genet. 2017;26(16):3031-3045. doi:10.1093/hmg/ddx140

Acknowledgements

First, I would like to thank Prof. Karl-Ludwig Laugwitz and Prof. Alessandra Moretti for giving me the opportunity to work in their group. I am deeply thankful for the support and guidance I received during this time.

This project was a fascinating journey into the molecular mechanisms of heart development that deeply benefited from continuous sharing of ideas and experimental findings among group members and external collaborators, eventually leading to the final picture that we now have.

A big thank you goes to the all the lab members, Svenja, Tatjana, Luna, Jessy, Zhifen, Birgit and Christina. I will always recall with affection the time I spent with you all in Munich.

But the biggest thank you goes to my parents and my brother, for always encouraging me in my career path and supporting unconditionally all my movings from Italy to Germany.